Article

Cell Reports

eIF4A3 Phosphorylation by CDKs Affects NMD during the Cell Cycle

Graphical Abstract

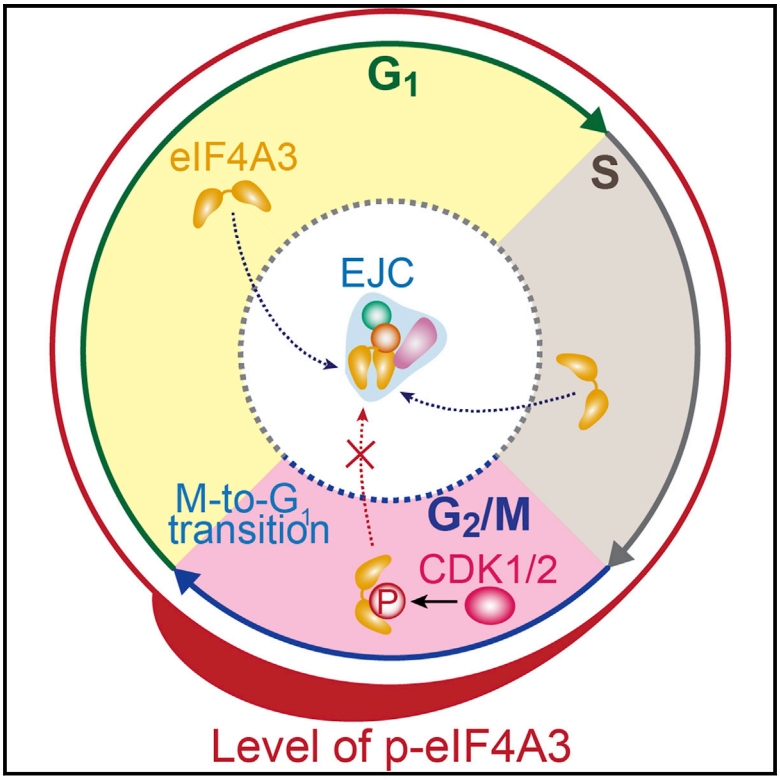

Authors

Incheol Ryu, You-Sub Won, Hongseok Ha, ..., Hyun Kyu Song, Hosung Jung, Yoon Ki Kim

Correspondence

yk-kim@korea.ac.kr

In Brief

Ryu et al. show that eIF4A3 (a core EJC component) is phosphorylated at the threonine 163 position by CDK1 and CDK2 in a cell cycle-dependent manner. This event triggers EJC remodeling and affects NMD efficiency in a cell cycle-dependent manner.

Highlights

- eIF4A3 is phosphorylated at threonine 163 by CDK1 and CDK2
- T163 phosphorylation triggers EJC remodeling
- T163 phosphorylation affects NMD efficiency in a cell cycle-dependent manner
- T163 dephosphorylation promotes M-to-G_1 transition

Ryu et al., 2019, Cell Reports *26*, 2126–2139
February 19, 2019
https://doi.org/10.1016/j.celrep.2019.01.101

CellPress

OPEN ACCESS
CellPress

Cell Reports
Article

eIF4A3 Phosphorylation by CDKs Affects NMD during the Cell Cycle

Incheol Ryu,[1,2,4] You-Sub Won,[1,2,4] Hongseok Ha,[1,2] Eunjin Kim,[3] Yeonkyoung Park,[1,2] Min Kyung Kim,[2] Do Hoon Kwon,[2] Junho Choe,[2] Hyun Kyu Song,[2] Hosung Jung,[3] and Yoon Ki Kim[1,2,5,*]

[1]Creative Research Initiatives Center for Molecular Biology of Translation, Korea University, Seoul 02841, Republic of Korea
[2]Division of Life Sciences, Korea University, Seoul 02841, Republic of Korea
[3]Brain Korea 21 PLUS Project for Medical Science, Department of Anatomy, and Brain Research Institute, Yonsei University College of Medicine, Seoul 02841, Republic of Korea
[4]These authors contributed equally
[5]Lead Contact
*Correspondence: yk-kim@korea.ac.kr
https://doi.org/10.1016/j.celrep.2019.01.101

SUMMARY

Exon junction complexes (EJCs) loaded onto spliced mRNAs during splicing serve as molecular markers for various post-transcriptional gene-regulatory processes, including nonsense-mediated mRNA decay (NMD). Although the composition and structure of EJCs are well characterized, the mechanism regulating EJC deposition remains unknown. Here we find that threonine 163 (T163) within the RNA-binding motif of eIF4A3 (a core EJC component) is phosphorylated by cyclin-dependent protein kinases 1 and 2 in a cell cycle-dependent manner. T163 phosphorylation hinders binding of eIF4A3 to spliced mRNAs and other EJC components. Instead, it promotes association of eIF4A3 with CWC22, which guides eIF4A3 to an active spliceosome. These molecular events ensure the fidelity of specific deposition of the EJC ~20–24 nt upstream of an exon-exon junction. Accordingly, NMD is affected by T163 phosphorylation. Collectively, our data provide evidence that T163 phosphorylation affects EJC formation and, consequently, NMD efficiency in a cell cycle-dependent manner.

INTRODUCTION

Messenger ribonucleoproteins (mRNPs) are continuously remodeled throughout their whole lifetime, from mRNA synthesis to mRNA degradation (Singh et al., 2015). In metazoan cells, a pivotal protein component of mRNPs is the exon junction complex (EJC), which is deposited onto an mRNA ~20–24 nt upstream of an exon-exon junction as a consequence of a splicing event in the nucleus (Le Hir et al., 2000). The EJC serves as a molecular marker of proper splicing of intron-containing pre-mRNAs and concomitantly influences various essential steps of gene expression (Boehm and Gehring, 2016; Le Hir et al., 2016; Woodward et al., 2017; additional references therein). In the nucleus, an EJC deposited onto a partially spliced pre-mRNA affects splicing of flanking introns. In addition, the EJC enhances mRNP export from the nucleus to the cytoplasm and promotes translation of spliced mRNAs there. The EJC also triggers nonsense-mediated mRNA decay (NMD), by which transcripts harboring a premature translation termination codon (PTC) are selectively degraded (Hug et al., 2016; Karousis et al., 2016; Kim and Maquat, 2019). Furthermore, proper spatiotemporal localization of a subset of mRNAs in *Drosophila* oocytes is ensured by the EJC (Hachet and Ephrussi, 2004).

The EJC is a multiprotein complex composed of four core proteins and several peripheral proteins (Boehm and Gehring, 2016; Le Hir et al., 2016; Woodward et al., 2017). The core proteins are eukaryotic translation initiation factor 4A3 (eIF4A3), metastatic lymph node 51 (MLN51, also known as barentsz or CASC3), Y14 (also known as RNA-binding motif 8A), and mago nashi homolog (MAGOH). In the EJC core, eIF4A3 is at the center of a network of interactions. Structural analysis has revealed that eIF4A3 has two states depending on the arrangement of its two RecA-like domains: an open conformation of free or MLN51-bound eIF4A3 and a closed conformation in the EJC (Andersen et al., 2006; Bono et al., 2004, 2006). In the open conformation, eIF4A3 has weak binding activity toward RNA. In the closed conformation, however, the two RecA-like domains are in close proximity and form a deep cleft, providing the binding sites for ATP and RNA. MLN51 wraps around eIF4A3 and interacts with a heterodimer of MAGOH and Y14, which also binds to the interdomain cleft of eIF4A3, stabilizing the closed conformation of eIF4A3.

The deposition of a core EJC on an mRNA is initiated at an early step of splicing via a CWC22-mediated mechanism linking a splicing event to a step for the recruitment of eIF4A3 to mRNA (Alexandrov et al., 2012; Barbosa et al., 2012; Buchwald et al., 2013; Steckelberg et al., 2012). The direct interaction between CWC22 and eIF4A3 maintains eIF4A3 in the open conformation, which is unfavorable for binding of eIF4A3 to ATP and mRNA and, presumably, delivers eIF4A3 to an active spliceosome. Then, a transition of eIF4A3 from the open to the closed conformation allows eIF4A3 to clamp the RNA with the help of a heterodimer of MAGOH and Y14 as well as MLN51. The resulting EJC properly deposited onto the spliced mRNA triggers effective mRNP export from the nucleus to the cytoplasm.

In the cytoplasm, EJCs are released from mRNAs under the influence of PYM (partner of Y14 and MAGOH) in a translation-dependent manner (Gehring et al., 2009). PYM binds to the

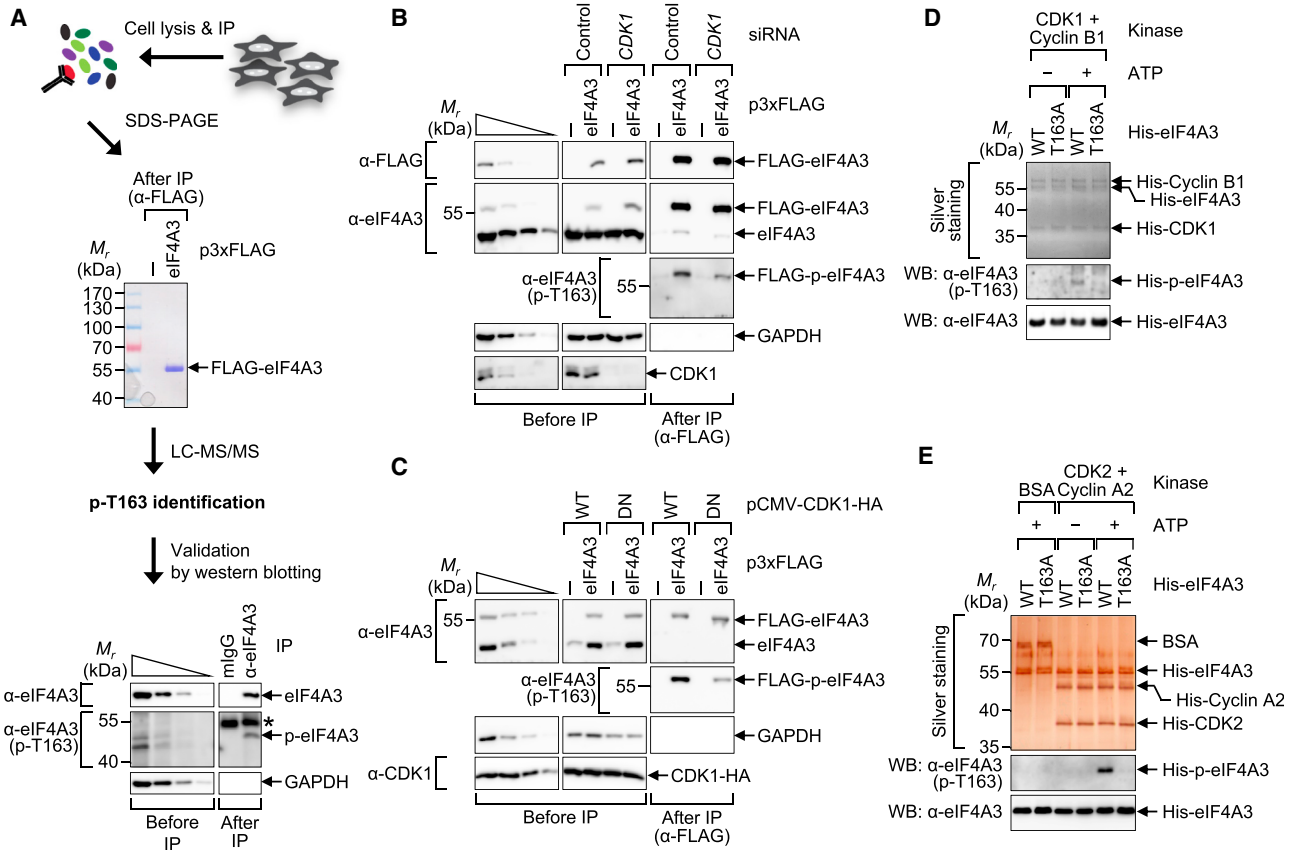

Figure 1. CDK1 and CDK2 Phosphorylates the T163 Residue of eIF4A3

(A) Experimental schematic for identification of possible phosphorylation sites within human eIF4A3 in HEK293T cells. Immunopurified FLAG-eIF4A3 was analyzed by SDS-PAGE (center) and LC-MS/MS. Specific phosphorylation at T163 was demonstrated by western blotting with a lab-made antibody against eIF4A3 phosphorylated at T163 (bottom). To demonstrate that western blotting was semiquantitative, 3-fold serial dilutions of total cell extracts were loaded in the four leftmost lanes. The immunoglobulin heavy chain is indicated by an asterisk.

(B) IP of FLAG-eIF4A3 using extracts of cells depleted of endogenous CDK1. Representative images from two biological replicates (n = 2) are shown.

(C) IP of FLAG-eIF4A3 using extracts of cells overexpressing CDK1-HA-WT or -DN; n = 3.

(D) An *in vitro* kinase assay involving a purified recombinant CDK1-cyclin B1 complex and either His-eIF4A3-WT or -T163A. The relative amount and integrity of each protein were demonstrated by silver staining. The extent of T163 phosphorylation was determined by western blotting (WB) with the anti-p-eIF4A3 antibody. n = 2.

(E) An *in vitro* kinase assay by means of the purified recombinant CDK2-cyclin A2 complex and either His-eIF4A3-WT or -T163A; n = 2.

See also Figure S1.

Y14-MAGOH complex and to the small subunit of a ribosome via its N-terminal and C-terminal region, respectively. When an elongating ribosome encounters an EJC, the ribosome-associated PYM interacts with Y14-MAGOH, disrupting the interaction between eIF4A3 and Y14-MAGOH. This mutually exclusive interaction promotes disassembly of the EJC and dissociation of its components from mRNA (Andersen et al., 2006; Bono et al., 2004, 2006; Gehring et al., 2009).

Although abundant data regarding the composition and structure of EJCs are available, the molecular basis of the mechanism regulating EJC assembly and disassembly is currently unclear. In this study, we provide evidence that the threonine 163 residue (T163) positioned in the RNA-binding motif of eIF4A3 is phosphorylated by cyclin-dependent protein kinases 1 and 2 (CDK1 and CDK2) in a cell cycle-dependent manner. These events trigger EJC remodeling and, consequently, affect NMD efficacy during the cell cycle, highlighting the effect of the regulation of eIF4A3 phosphorylation on EJC remodeling.

RESULTS

eIF4A3 Is Phosphorylated at the Threonine 163 Residue

To investigate possible post-translational modifications in eIF4A3 (a core component of the EJC), we carried out immunoprecipitation (IP) using HEK293T cells expressing FLAG-eIF4A3 (Figure 1A). The immunopurified FLAG-eIF4A3 band was then excised and subjected to liquid chromatography-tandem mass spectrometry (LC-MS/MS). The LC-MS/MS results identified a single phosphorylated site at the threonine 163 (T163) position at a coverage rate of 90% (50 peptides; Figure S1A). The specific

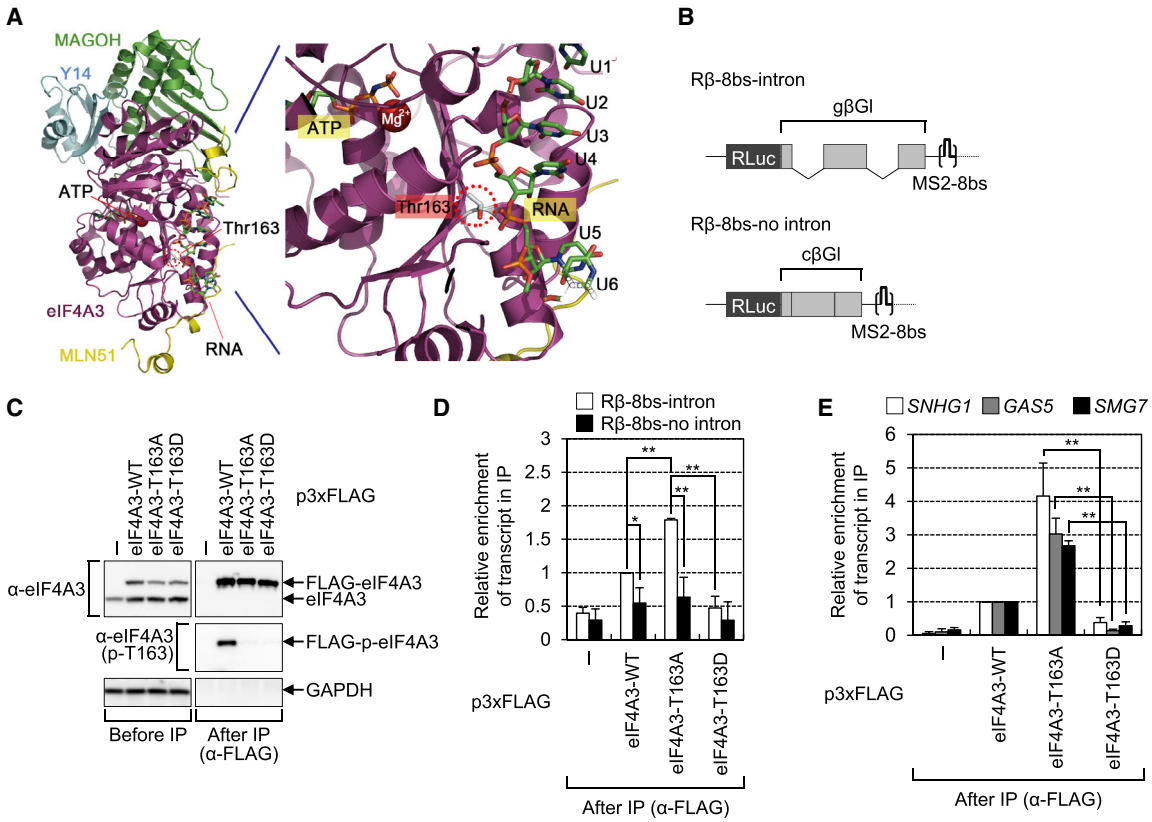

Figure 2. T163 Phosphorylation Disrupts the RNA-Binding Ability of eIF4A3

(A) Structure of an EJC complex with bound RNA (PDB: 2HYI). Left: ribbon diagrams of eIF4A3, MLN51, Y14, and MAGOH are shown in purple, yellow, cyan, and green, respectively. Bound RNA and ATP molecules are shown as stick models. Right: a close-up view of the RNA-binding region of eIF4A3. A bound magnesium ion is presented as a red ball. The T163 residue is indicated by a red dotted circle. The positions of six ribonucleotides (uridylates) are indicated as "U1–U6."

(B) A schematic diagram of the Rβ-8bs-intron and Rβ-8bs-no intron reporter mRNAs. RLuc, *Renilla* luciferase; gβGl and cβGl, genomic and intronless DNA sequences of β-globin, respectively; MS2-8bs, eight tandem repeats of bacteriophage MS2-binding sites.

(C and D) IPs of FLAG-eIF4A3-WT, -T163A, or -T163D with an anti-FLAG antibody in the extracts of HEK293T cells transiently expressing either FLAG-eIF4A3-WT or its mutant, pGL3-control expressing intronless firefly luciferase (FLuc) mRNA, and either Rβ-8bs-intron or Rβ-8bs-no intron reporter mRNA.

(C) Comparable IPs and specific phosphorylation of FLAG-eIF4A3.

(D) The levels of coimmunopurified reporter mRNAs were normalized to the level of coimmunopurified FLuc mRNAs. The normalized level in the IP from the extracts of cells expressing FLAG-eIF4A3-WT and Rβ-8bs-intron was arbitrarily set to 1.0. Two-tailed and equal-variance Student's t test was carried out for statistical analysis; *$p < 0.05$, **$p < 0.01$; $n = 3$.

(E) Association between eIF4A3 and endogenous transcripts containing multiple introns; as in (D), except that the amounts of coimmunopurified endogenous transcripts were normalized to the level of coimmunopurified endogenous intronless histone H2A mRNA. **$p < 0.01$, $n = 3$.

See also Figure S2.

phosphorylation of endogenous eIF4A3 at T163 was next confirmed by western blotting using immunopurified endogenous eIF4A3 and a lab-made anti-phospho (p)-specific eIF4A3 antibody (Figure 1A, bottom). Of note, our anti-p-eIF4A3 antibody yielded one nonspecific band (below p-eIF4A3) in the samples before IP. Nevertheless, the nonspecific band disappeared after the sample was subjected to IP of endogenous eIF4A3. Therefore, to minimize the nonspecific band throughout our present study, we always determined the amount of p-eIF4A3 by western blotting involving immunopurified endogenous or FLAG-tagged eIF4A3. Indeed, our anti-p-eIF4A3 antibody reacted with immunopurified FLAG-eIF4A3 but not with immunopurified FLAG-eIF4A1 (Figure S1B), which is highly similar to eIF4A3 in the amino acid sequence (Li et al., 1999), thus indicating high specificity of the anti-p-eIF4A3 antibody (see also Figure 2C; our anti-p-eIF4A3 antibody reacted only with FLAG-eIF4A3-wild-type [WT], not with FLAG-eIF4A3-T163A or FLAG-eIF4A3-T163D).

CDK1 and CDK2 Trigger T163 Phosphorylation of eIF4A3

Existing phosphoproteomics data have shown possible phosphorylation of eIF4A3 by CDKs (Chi et al., 2008; Dephoure et al., 2008). Therefore, we tested whether CDKs induce eIF4A3 phosphorylation at T163. First, downregulation of CDK1 (Figure 1B) or CDK2 (Figure S1C) via a specific small interfering RNA (siRNA) reduced T163 phosphorylation of immunopurified FLAG-eIF4A3. Second, overexpression of a dominant-negative (DN) form of CDK1 (Figure 1C) or CDK2 (Figure S1D) drastically

reduced T163 phosphorylation of immunopurified FLAG-eIF4A3. Third, the purified recombinant complexes CDK1-cyclin B1 (Figure 1D) and CDK2-cyclin A2 (Figure 1E), but not CDK2-cyclin E1 (Figure S1E) or BSA (Figure 1E), triggered (in an ATP-dependent manner) phosphorylation of purified recombinant WT eIF4A3 (hereafter called eIF4A3-WT), but not of eIF4A3-T163A, which contained a single amino acid substitution of threonine (T) with alanine (A) at position 163 (preventing phosphorylation). All *in vivo* and *in vitro* data indicate that CDK1-cyclin B1 and CDK2-cyclin A2 phosphorylate eIF4A3 on the T163 residue. In support of this conclusion, the amino acid sequence around T163 of eIF4A3 (i.e., sequence pTPGR) perfectly matches the consensus sequence of the phosphorylation site of a CDK substrate: [p(S/T)PX(K/R)] (Bertoli et al., 2013; Hydbring et al., 2016).

T163 Phosphorylation Hinders Binding of eIF4A3 to Spliced mRNAs

In an EJC, six ribonucleotides are in contact with eIF4A3 on the surface opposite the ATP-binding site of the EJC (Andersen et al., 2006; Bono et al., 2004, 2006). Notably, the fifth phosphate, which links the fourth and fifth ribonucleotides, comes into direct contact with eIF4A3 T163 (Figure 2A), which corresponds to the phosphorylation site identified in this study (Figure 1). These observations raised the possibility that T163 phosphorylation may affect the RNA-binding ability of eIF4A3.

To verify this possibility, we employed two reporter mRNAs, Rβ-8bs-intron and Rβ-8bs-no intron (Figure 2B), encoding *Renilla* luciferase (RLuc) followed by either the genomic or intronless sequence of the β-globin (*βGl*) gene, respectively, and eight tandem repeats of bacteriophage MS2-binding sites (8bs) in the 3′ UTR. The two reporter plasmids were expected to express mRNAs of identical sequences. Nonetheless, Rβ-8bs-intron mRNA should carry two EJCs because of the presence of two introns. On the contrary, Rβ-8bs-no intron mRNA should have no EJCs.

Next, we conducted RNA-IP experiments by means of the reporter mRNAs to assess the RNA-binding ability of eIF4A3-WT and its mutants T163A and T163D, in which T163 was replaced by neutral alanine (A) or aspartic acid (D) to prevent or mimic phosphorylation, respectively. Comparable IP efficacy and specific phosphorylation were confirmed by western blotting (Figure 2C). Analysis of coimmunopurified mRNAs revealed that Rβ-8bs-intron mRNA was preferentially enriched in the IPs of FLAG-eIF4A3-WT and -T163A compared with Rβ-8bs-no intron mRNA (Figure 2D). Moreover, a greater amount of Rβ-8bs-intron mRNA coimmunopurified with FLAG-eIF4A3-T163A than with FLAG-eIF4A3-WT. On the contrary, only a marginal amount of Rβ-8bs-intron mRNA coimmunopurified with the T163D mutant. In line with these results, greater amounts of the endogenous transcripts containing multiple introns (that is, endogenous transcripts bound to multiple EJCs after splicing) were observed in the IP of the T163A mutant in comparison with that of WT eIF4A3 (Figure 2E): small nucleolar RNA host gene 1 (*SNHG1*) RNA, growth arrest-specific 5 (*GAS5*) RNA, and *SMG7* mRNA; the first two of the three are noncoding RNAs (ncRNAs). In contrast, the endogenous transcripts barely coimmunopurified with the T163D mutant.

The inhibitory effect of T163 phosphorylation on the association between eIF4A3 and spliced mRNAs was further confirmed by a reduction in the amounts of copurified FLAG-eIF4A3-T163D, relative to FLAG-eIF4A3-T163A, in an RNA pull-down assay using maltose-binding protein (MBP; Figures S2A and S2B). All of these data indicate that T163 phosphorylation hinders the association between eIF4A3 and a spliced (intron-containing) mRNA. Of note, eIF4A3-WT and its mutants manifested nuclear distribution (Figure S2C), indicating that the phosphorylation itself does not significantly affect the nuclear localization of eIF4A3.

Phosphorylated eIF4A3 Fails to Form an EJC

We next wondered whether elimination of the RNA-binding ability of eIF4A3 by T163 phosphorylation affects EJC assembly. To address this question, we performed IPs on cells expressing either FLAG-eIF4A3-WT or one of its mutants (Figure 3A). The cell extracts were either left untreated or treated with RNase A before IP. Similarity of expression as well as IP efficacy of FLAG-eIF4A3 (either WT or mutants) were confirmed by western blotting. In addition, efficient removal of cellular RNAs by RNase A treatment was evident because of almost complete elimination of endogenous *GAPDH* mRNAs (Figure S3A). The IP data showed that all EJC core components coimmunopurified with FLAG-eIF4A3-WT and -T163A but not with FLAG-eIF4A3-T163D. In addition, cap-binding protein 80 (CBP80), but not eukaryotic translation initiation factor 4E (eIF4E), was preferentially enriched in IPs of FLAG-eIF4A3-WT and -T163A but not in the IP of FLAG-eIF4A3-T163D. In agreement with these data, the EJC is known to preferentially associate with a newly synthesized mRNA bound to a nuclear cap-binding complex (a heterodimer of CBP80 and CBP20) rather than with a cytoplasmic cap-binding protein, eIF4E (Lejeune et al., 2002). Of note, all of the observed interactions were resistant to RNase A treatment, pointing to an RNA-independent association. Furthermore, reciprocal IPs in the extracts of cells transiently expressing λN-hemagglutinin (HA)-fused GFP, λN-HA-Y14, or λN-HA-MAGOH showed that FLAG-eIF4A3-WT and -T163A, but not -T163D, coimmunopurified with λN-HA-Y14 and λN-HA-MAGOH (Figure S3B). All of these data indicate that p-eIF4A3 fails to form an EJC.

T163 Phosphorylation by CDKs Occurs in the Cytoplasm after EJC Disassembly

We next investigated where and when T163 phosphorylation takes place. First, the results of IPs using the cytoplasmic extracts revealed that, when PYM was overexpressed, ~27-fold more endogenous PYM (which is known to trigger EJC disassembly; Gehring et al., 2009), the amount of cytoplasmic p-eIF4A3 increased 2.1-fold (Figures 3B and S3C). Second, the results of IPs using the cytoplasmic extracts of CDK1-depleted cells revealed that downregulation of CDK1 reduced the level of cytoplasmic p-eIF4A3 by 2.2-fold (Figures S3D and S3E). Third, treatment of the cells with puromycin, which is a potent translation inhibitor (and, consequently, inhibits EJC disassembly by an elongating ribosome), reduced the amount of cytoplasmic p-eIF4A3 ~2.5-fold (Figure S3F). Taken together, these

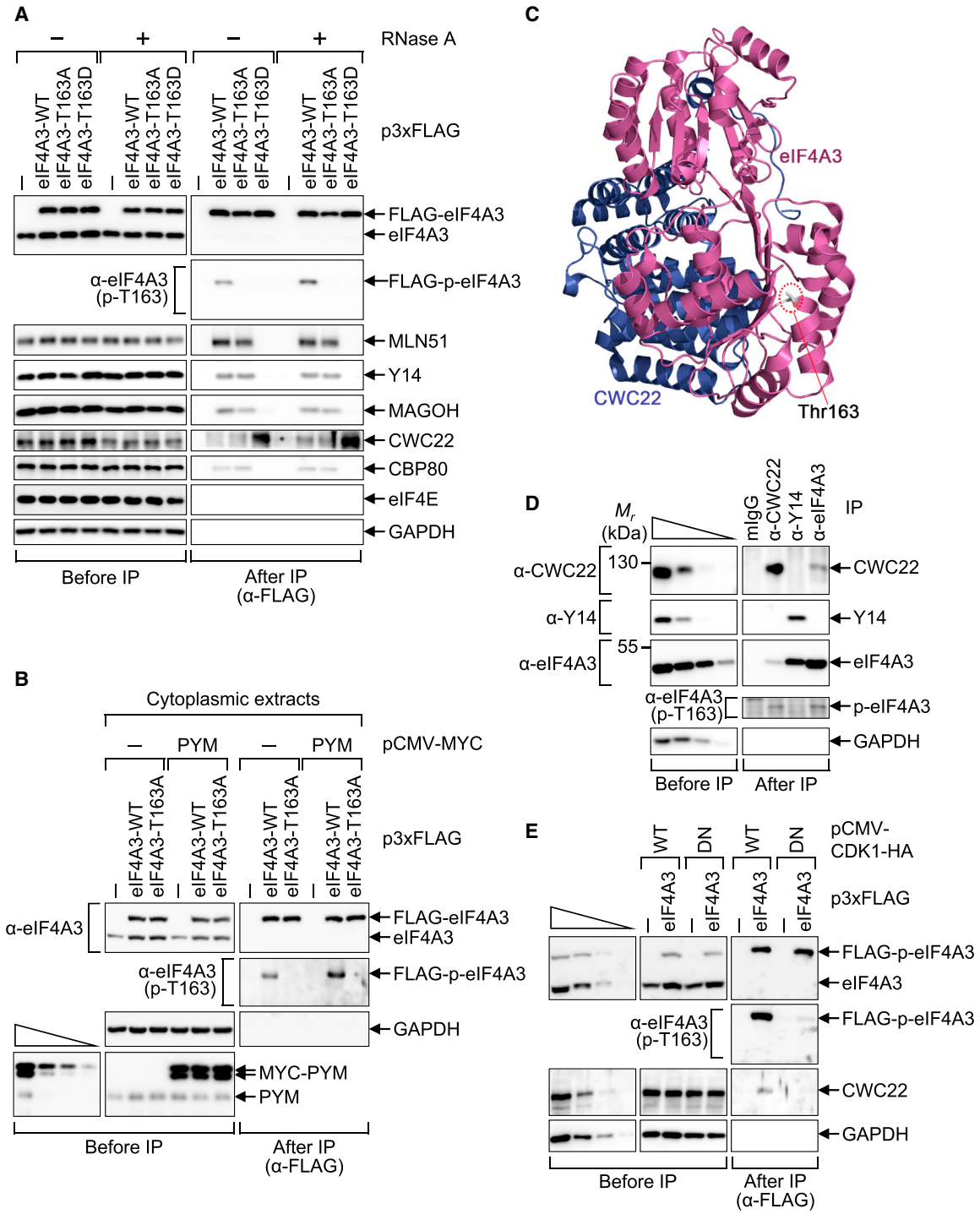

Figure 3. T163 Phosphorylation of eIF4A3 Triggers EJC Remodeling

(A) IPs of FLAG-eIF4A3-WT and its mutants. The IPs were performed using anti-FLAG antibody and extracts of HEK293T cells transiently expressing FLAG-eIF4A3-WT or one of its mutants and either untreated or treated with RNase A. n = 4.

(B) IPs of FLAG-eIF4A3 in cytoplasmic extracts of cells overexpressing MYC-PYM; n = 2.

(C) The structure of eIF4A3 in complex with CWC22 (PDB: 4C9B). Ribbon diagrams of eIF4A3 and CWC22 are shown in purple and blue, respectively. Residue T163 is indicated by a red dotted circle.

(D) Preferential association of p-eIF4A3 with CWC22. IPs were performed with an antibody against endogenous CWC22, Y14, or eIF4A3. n = 2.

(E) IPs of FLAG-eIF4A3-WT in cells overexpressing either WT or DN CDK1-HA; n = 3.

See also Figure S3.

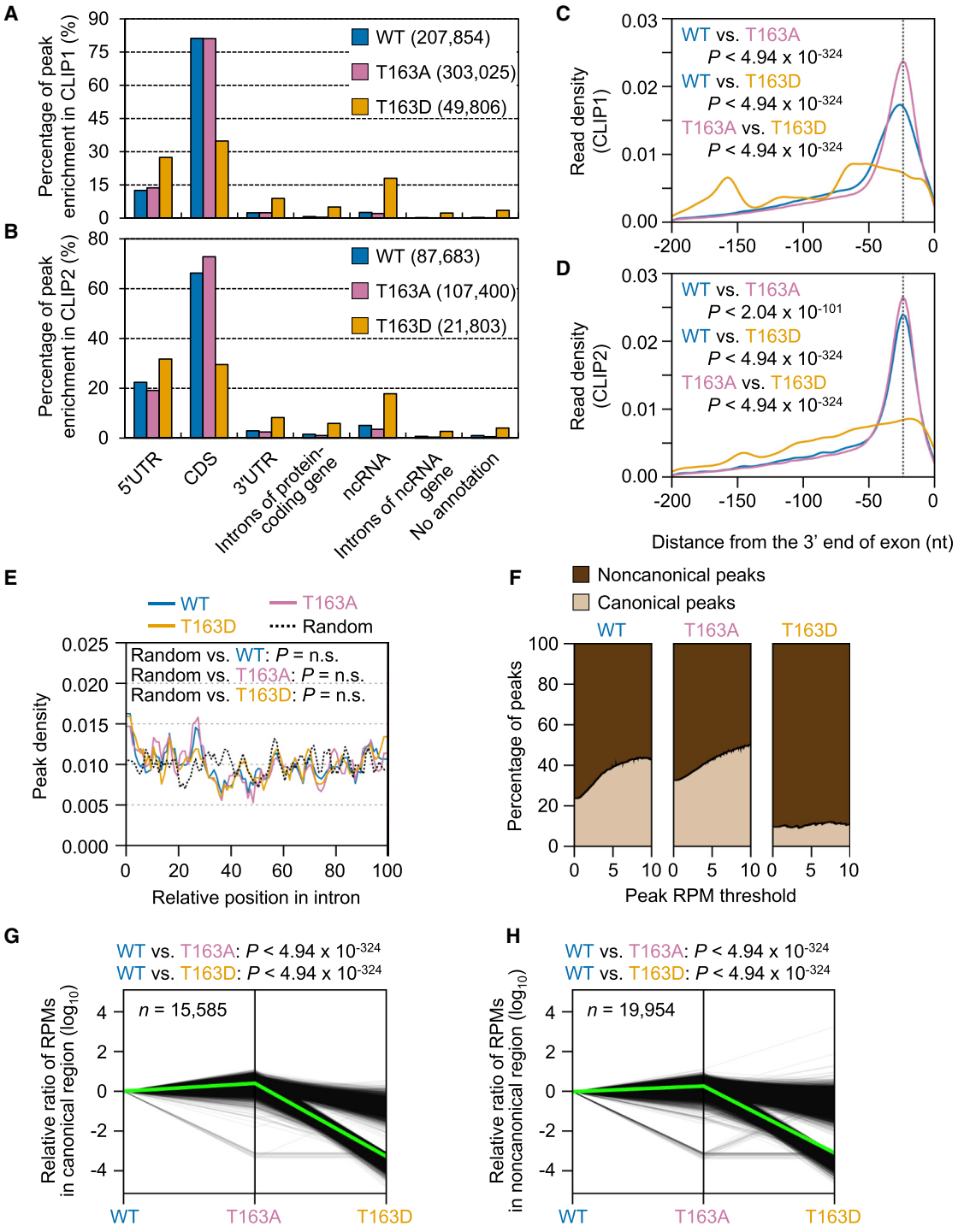

Figure 4. T163 Phosphorylation Abrogates Position-Dependent Loading of eIF4A3 ~24 nt Upstream of 3′ Ends of Exons

(A and B) Relative distributions of peaks adjusted for nucleotide length of the regions. The data obtained from two biological replicates of CLIP-seq experiments were analyzed: (A) CLIP1 and (B) CLIP2. The number of peaks mapped to each region was divided by the percentage of nucleotides of each region in the genome. The numbers of the called peaks from each CLIP-seq experiment are presented in parentheses.

(C and D) The distribution of the centers of uniquely mapped reads from CLIP1 (C) and CLIP2 (D) data with reference to the 3′ ends of the exons of CDSs. The p values were computed by two-sided Kolmogorov-Smirnov test.

(E) Relative distribution of the centers of overlapping peaks located in the introns from two biological replicates of CLIP-seq experiments. Each intron was binned into 50 segments. The p values were computed by two-sided Kolmogorov-Smirnov test. n.s., not significant.

(legend continued on next page)

data suggest that eIF4A3 is phosphorylated by CDK1 and/or possibly CDK2 after EJC disassembly in the cytoplasm.

T163 Phosphorylation Promotes an Association between eIF4A3 and CWC22

Because the nuclear localization of eIF4A3 was not affected by T163 phosphorylation (Figure S2C), the eIF4A3 phosphorylated by CDKs in the cytoplasm after EJC disassembly may efficiently enter the nucleus for recycling. CWC22 directly interacted with eIF4A3 with an open conformation (Figure 3C) and is known to guide it toward an active spliceosome in the nucleus (Alexandrov et al., 2012; Barbosa et al., 2012; Buchwald et al., 2013; Steckelberg et al., 2012). Therefore, it is likely that T163 phosphorylation may have an influence on the interaction between eIF4A3 and CWC22.

The IP results revealed that endogenous p-eIF4A3 was preferentially enriched in the IP of CWC22, not that of Y14 (Figure 3D). Furthermore, overexpression of a DN form of either CDK1 (Figure 3E) or CDK2 (Figure S3G) significantly reduced the amount of coimmunopurified CWC22 in the FLAG-eIF4A3 IP assay. In addition, CWC22 was preferentially enriched in the immunoprecipitates of FLAG-eIF4A3-T163D in an RNase A-resistant manner compared with the immunoprecipitates of FLAG-eIF4A3-WT or FLAG-eIF4A3-T163A (Figure 3A). These observations indicate that T163 phosphorylation of eIF4A3 promotes an association between eIF4A3 and CWC22.

Transcriptome-wide Effect of T163 Phosphorylation of eIF4A3

Next, to look for transcriptome-wide interactions between target transcripts and eIF4A3-WT, -T163A, or -T163D, we conducted two biologically independent cross-linking IP experiments coupled with high-throughput sequencing (CLIP-seq; CLIP1 and CLIP2) using eIF4A3-depleted HeLa cells expressing FLAG-eIF4A3-WT, -T163A, or -T163D (Figure 4). The specificity of IPs was confirmed by western blotting (Figure S4A). In CLIP1 and CLIP2, 42.8–44.9 and 42.5–43.7 million raw reads, respectively, were generated by high-throughput sequencing (Table S1). After adaptor sequence trimming in the CutAdapt software, removal of ribosomal sequences by means of RiboPicker, and mapping to the human reference genome sequence (hg19) using STAR Aligner, 3.9–9.1 and 1.7–3.3 million uniquely mapped reads were obtained in CLIP1 and CLIP2, respectively (Table S1). We then calculated Pearson correlation coefficients (r) between CLIP1 and CLIP2 for fragments per kilobase of transcript per million mapped reads (FPKM) per gene. All calculated Pearson correlation coefficients were greater than 0.807, indicating strong correlations between CLIP1 and CLIP2 (Figures S4B–S4D).

To assess potential differences in the binding of eIF4A3-WT, -T163A, and -T163D to different regions of transcripts, we next performed peak calling in the CLIP1 and CLIP2 data by means of the Piranha software (Uren et al., 2012). According to the mapped positions of the peaks on transcripts, the called peaks were categorized into the following seven regions: 5′ UTRs, coding sequences (CDSs), 3′ UTRs, introns of a protein-coding gene, ncRNAs, introns of ncRNA genes, and "no annotation." The relative distributions of the called peaks adjusted for the nucleotide length of the regions yielded preferential mapping of the peaks from CLIPs of eIF4A3-WT and -T163A to CDSs compared with those of the CLIP of T163D (Figures 4A and 4B). In addition, the peaks from CLIPs of eIF4A3-WT and -T163A were more enriched in the 5′ UTR than in the 3′ UTR (5.2- and 5.7-fold in CLIP1, respectively [Figure 4A]; 7.6- and 7.8-fold in CLIP2, respectively [Figure 4B]). In support of this finding, one report has shown that 5′ UTRs contain 3-fold more introns than 3′ UTRs (Bicknell et al., 2012).

T163 Phosphorylation Hinders Position-Dependent Loading of eIF4A3 onto a CDS

We further analyzed the CLIP-seq data to narrow down the eIF4A3-binding sites in CDSs. For this purpose, the centers of the uniquely mapped reads, which mapped to the exons of CDSs, were analyzed. After that, the centers were plotted with reference to the 3′ ends of the exons of CDSs. In agreement with previous transcriptome-wide analyses of eIF4A3-binding sites (Hauer et al., 2016; Saulière et al., 2012; Singh et al., 2012), we observed preferential enrichment of the uniquely mapped reads from eIF4A3-WT CLIP or T163A CLIP at sites ~24 nt upstream of the 3′ ends of the exons of CDSs (Figures 4C and 4D for CLIP1 and CLIP2, respectively). On the contrary, the uniquely mapped reads from T163D CLIP manifested marginal enrichment at those sites; it is most likely that these reads were due to a nonspecific or basal association of eIF4A3-T163D with RNAs. A similar analysis of the overlapping peaks located in introns of protein-coding genes from two independent CLIP experiments (Table S1) revealed no preferential enrichment in introns compared with a random distribution (Figure 4E), indicating a nonspecific association between eIF4A3 (WT, T163A, and T163D) and introns under our conditions.

eIF4A3 may bind to a noncanonical region (as either a free molecule or a component of the EJC) or to a canonical region (Saulière et al., 2012; Singh et al., 2012). Therefore, we next compared the percentages of canonical and noncanonical peaks located in the exons of protein-coding genes among CLIPs of eIF4A3-WT, -T163A, and -T163D. To this end, the overlapping peaks from two independent CLIP experiments (Table S1) were categorized into two groups: "canonical peak" (peaks located between 40 and 10 nt upstream of exon-exon junctions) and "noncanonical peak" (peaks located elsewhere in exons). As the thresholds for reads per million mapped reads (RPMs) of the peaks increased from 0 to 10, the percentage of canonical peaks gradually increased from 20% to 50% in eIF4A3-WT CLIP and T163A CLIP (Figure 4F), in line with one report showing that

(F) Percentages of canonical and noncanonical peaks mapped to an exonic region according to different thresholds for peak RPMs.
(G and H) Relative number of RPMs of reads mapped to an individual canonical (G) and noncanonical (H) exonic region. The RPMs of reads from eIF4A3-WT CLIP were arbitrarily set to 1.0 (0 on a $\log_{10}$ scale). The thick green lines indicate a median value (0.39 and −3.20 for T163A and T163D in G, respectively; 0.28 and −3.01 for T163A and T163D in H, respectively). The p values were calculated by one-tailed Mann-Whitney U test.
See also Figure S4 and Table S1.

half of the peaks from eIF4A3-WT CLIP are located in the canonical region (Saulière et al., 2012). In contrast, the percentage of canonical peaks in the T163D CLIP remained ~10%. These data indicate that a significant proportion of eIF4A3 peaks obtained in eIF4A3-WT CLIP and eIF4A3-T163A CLIP, but not eIF4A3-T163D CLIP, are enriched at canonical EJC sites.

Further analysis of the canonical and noncanonical peaks revealed a purine-rich motif, GAAGA or AAGAA, as the predominant RNA motif for eIF4A3 binding (Figure S4E), in agreement with another report (Saulière et al., 2012). In addition, the RPMs of the reads from eIF4A3-WT CLIP and T163A CLIP that mapped to a canonical (Figure 4G) or noncanonical (Figure 4H) exonic region of individual protein-coding genes were substantially lower in the T163D CLIP; the median values (on a $\log_{10}$ scale) of a ratio of eIF4A3-WT CLIP to T163A CLIP and eIF4A3-WT CLIP to T163D CLIP were 0.39 and −3.20 in canonical regions and 0.28 and −3.01 in noncanonical regions, respectively. Selected examples of canonical peaks also showed preferential enrichment of eIF4A3-WT and -T163A and marginal enrichment of eIF4A3-T163D 24 nt upstream of exon-exon junctions (Figure S4F). Altogether, these data suggest that T163 phosphorylation hinders the binding of eIF4A3 to RNA at canonical and noncanonical EJC sites, disrupting the preferential deposition of eIF4A3 ~24 nt upstream of 3′ ends of exons.

T163 Phosphorylation Inhibits NMD

Considering that EJCs play a crucial role in NMD, the molecular events (characterized above) that were caused by T163 phosphorylation might have an effect on NMD. To test this possibility, we first generated HeLa cell lines that expressed siRNA-resistant and doxycycline (Dox)-inducible FLAG-eIF4A3-WT, -T163A, or -T163D. Then, using these cell lines, we analyzed NMD efficiency by measuring the levels of exogenously expressed NMD reporter mRNAs (*β-Gl* and *GPx1* mRNAs that were either harboring [Ter] or not harboring [Norm] a PTC) and endogenous NMD substrates. Specific downregulation of endogenous eIF4A3 by siRNA and comparable induction of FLAG-eIF4A3 relative to endogenous eIF4A3 by addition of Dox were confirmed by western blotting (Figure S5A). The results revealed that eIF4A3 downregulation significantly increased the amounts of exogenously expressed NMD reporter mRNAs (Figures 5A and 5B) and of endogenous NMD substrates (Figure 5C). Moreover, the observed increase was significantly reversed by induction of FLAG-eIF4A3-WT and -T163A, but not -T163D, via Dox treatment.

We next assessed differentially expressed genes (DEGs) in two biological replicates of mRNA sequencing of total RNA samples obtained from HeLa cell lines that were either undepleted or depleted of eIF4A3 and expressed inducible FLAG-eIF4A3-WT, -T163A, or -T163D (Figure S5B). The DEG analysis revealed that 1,406 and 1,365 genes were significantly upregulated and downregulated, respectively, at least 1.5-fold ($p < 0.05$) when the cells were depleted of eIF4A3 (Table S2). Moreover, the upregulation of DEGs was significantly reversed by induction of WT or T163A, but not T163D, in our analysis of mRNA sequencing data (Figure 5D; Table S3) and in validation experiments (Table S4). Furthermore, the levels of NMD substrates experimentally determined in another transcriptome analysis (Yepiskoposyan et al., 2011) were significantly higher after downregulation of eIF4A3, and this effect was reversed by induction of WT or T163A but not T163D (Figure 5E). All of these data indicate that T163 phosphorylation of eIF4A3 inhibits NMD.

The Level of p-eIF4A3 Varies throughout the Cell Cycle

We know that (1) the complexes CDK1-cyclin B and CDK2-cyclin alanine mainly function as M and S phase regulators, respectively (Bertoli et al., 2013; Hydbring et al., 2016), and (2) p-eIF4A3-dependent transcripts are significantly enriched with the gene ontology (GO) term "regulation of cell cycle" (Figure S5C; Tables S3 and S4). Therefore, our finding of eIF4A3 phosphorylation by CDK1 and CDK2 prompted us to test whether the level of eIF4A3 phosphorylation varies throughout the cell cycle. To this end, we employed HeLa cell lines that expressed siRNA-resistant and Dox-inducible FLAG-eIF4A3-WT (Figures 6A and S6A). Synchronization of the cells at the G_1-to-S transition by double thymidine block (DTB) and the proper release of the cell cycle after DTB removal were confirmed by fluorescence-activated cell sorting (FACS; Figure S6B) and western blotting with antibodies against CDKs and cyclins (Figures 6A and S6A, before IP). At the indicated time points after release, total cell extracts were prepared and subjected to IP by means of an antibody against FLAG. The amount of FLAG-p-eIF4A3 was determined by western blotting with an anti-p-eIF4A3 antibody. The results showed that the level of FLAG-p-eIF4A3 fluctuated depending on the cell cycle, with the highest level between late M and early G_1 phase (Figures 6A and S6A, after IP). It should be noted that a significant proportion of p-eIF4A3 remained during interphase.

We found that T163 phosphorylation hindered the RNA-binding ability of eIF4A3 (Figure 2) and promoted an association between eIF4A3 and CWC22 (Figure 3). On the basis of these observations, we next investigated whether all of these events were recapitulated in late M phase. For this purpose, we performed IPs on the extracts of inducible HeLa cells arrested either at the G_1-to-S transition (0 h) or in late M phase (16 h). The IP results showed that newly synthesized exogenously expressed Rβ-8bs-intron reporter mRNA was enriched in the immunoprecipitate of FLAG-eIF4A3 in late M phase 2.5-fold less in comparison with G_1-to-S transition (Figure 6B). In addition, 2.8-fold more CWC22 was enriched in the immunoprecipitate of FLAG-eIF4A3 in late M phase (Figure 6C). Collectively, these data suggest that T163 phosphorylation occurring in late M phase causes loss of the RNA-binding activity of eIF4A3 and promotes an association between eIF4A3 and CWC22.

T163 Dephosphorylation Promotes Effective M-to-G1 Transition

Which phase of the cell cycle is affected by T163 phosphorylation and dephosphorylation? To answer this question, we analyzed HeLa cell lines that express siRNA-resistant and Dox-inducible FLAG-eIF4A3-WT, -T163A, or -T163D. In these cell lines, we tested the effects of eIF4A3 downregulation and induction of eIF4A3-WT, -T163A, or -T163D on cell cycle progression (Figure 6D; see also Figure S6C for quantitation of the relative cell cycle distribution). FACS data revealed that, although there were no statistically significant effects at earlier time points, eIF4A3 downregulation delayed cell cycle progression 24 h after the release. The observed delay was partially reversed by induction

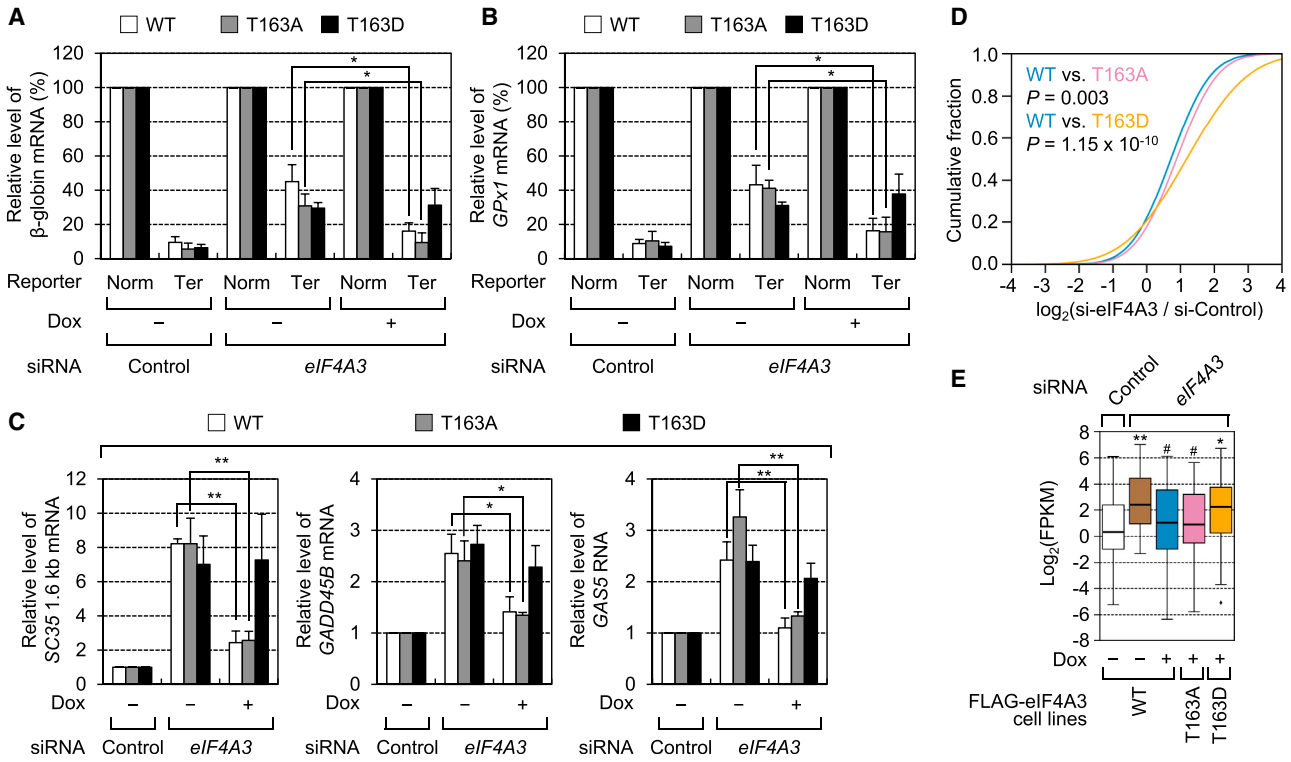

Figure 5. T163 Phosphorylation of eIF4A3 Affects NMD

(A–C) HeLa cells stably expressing siRNA-resistant Dox-inducible FLAG-eIF4A3-WT, -T163A, or -T163D were transiently transfected with either control siRNA or *eIF4A3* siRNA. One day after transfection, the cells were retransfected with (1) NMD reporter plasmids (pmCMV-Gl and pmCMV-GPx1) that were either PTC-free (Norm) or contained a PTC (Ter) and (2) the phCMV-MUP reference plasmid. One day later, the cells were harvested, and total cell RNA and protein were purified for analysis. FLAG-eIF4A3-WT, -T163A, or -T163D was induced by treatment with Dox for 2 days.

(A and B) NMD of reporter mRNAs. The levels of *Gl* (A) and *GPx1* (B) mRNAs were normalized to the level of *MUP* mRNA. Normalized levels of *Gl* Norm mRNA and *GPx1* Norm mRNA were arbitrarily set to 100%. *p < 0.05, n = 3.

(C) NMD of endogenous NMD substrates. The levels of endogenous NMD substrates were normalized to the amount of endogenous *GAPDH* mRNA. *p < 0.05, **p < 0.01, n = 3.

(D) Cumulative distribution function plots of the ratio of a transcript level after eIF4A3 downregulation to that after control downregulation to compare the effects of induced FLAG-eIF4A3-WT, -T163A, and -T163D. The DEGs upregulated at least 1.5-fold after eIF4A3 downregulation—with reversal by induction of FLAG-eIF4A3-WT—were analyzed. The p values were calculated by two-tailed Mann-Whitney *U* test.

(E) Boxplot analysis of experimentally determined NMD substrates. Among NMD substrates experimentally determined in a previous transcriptome analysis, the transcripts that were upregulated at least 1.5-fold after eIF4A3 downregulation—with reversal by induction of FLAG-eIF4A3-WT—were compared. The p values were calculated by two-tailed Mann-Whitney *U* test. *p < 0.05, **p < 0.01; #, not significant.

See also Figure S5 and Tables S2, S3, and S4.

of eIF4A3-WT or -T163A but not eIF4A3-T163D. Altogether, these data suggest that, although T163 dephosphorylation of eIF4A3 is not the main driver, T163 dephosphorylation promotes effective M-to-G_1 transition.

Cell Cycle-Dependent NMD Is Coupled to T163 Phosphorylation of eIF4A3

Given that T163 phosphorylation of eIF4A3 affected NMD (Figure 5) and that the level of T163 phosphorylation varied throughout the cell cycle (Figures 6A and S6A), we next wondered whether NMD efficiency varies by cell cycle phase. Because NMD largely targets newly synthesized mRNAs during the first (or pioneer) round of translation (Maquat et al., 2010; Ryu and Kim, 2017; Trcek et al., 2013), the newly synthesized mRNAs were labeled with 4-thiouridine (4SU). In addition, to rule out a possible transcription effect, the levels of the labeled RNAs were normalized to those of the corresponding pre-mRNAs. The qRT-PCR data revealed that the relative ratios of mRNAs to their pre-mRNAs of newly synthesized endogenous NMD substrates (Figure 7A) increased in late M phase and decreased in G_1 phase. Consistent with these results, the relative amounts of exogenously expressed NMD reporter mRNAs yielded a similar pattern (Figure 7B), indicating that NMD is repressed in late M phase and recovers in G_1 phase. Notably, the levels of intronless mRNAs and previously characterized EJC-independent NMD substrates (Chan et al., 2007) did not increase in late M phase (Figure S7). In addition, the expression levels of major NMD factors (UPF1, UPF2, and UPF3X) did not significantly change during the cell cycle (Figure S6A).

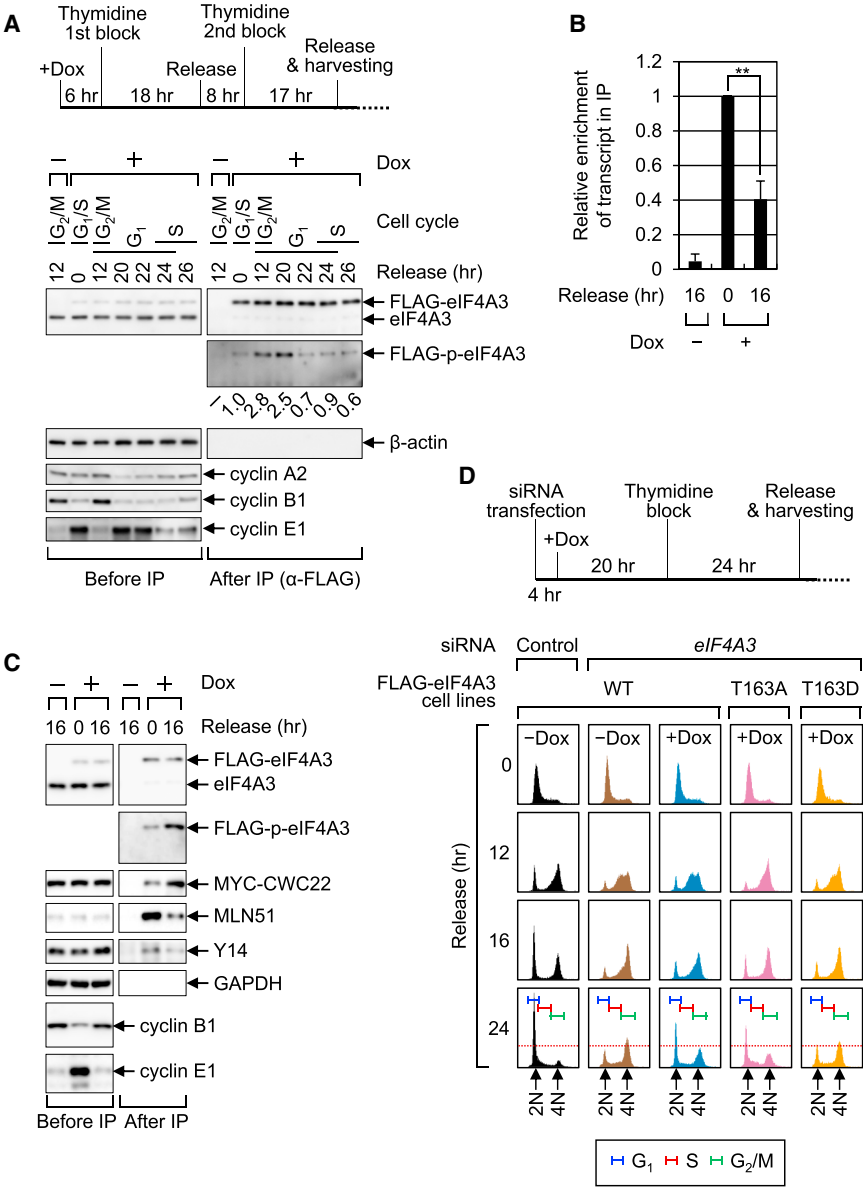

Figure 6. T163 Phosphorylation and Dephosphorylation Affect Cell Cycle Progression

(A) Cell cycle-dependent T163 phosphorylation of eIF4A3. HeLa cells expressing Dox-inducible FLAG-eIF4A3-WT were synchronized by DTB. FLAG-eIF4A3-WT was induced by treatment with Dox before DTB. Total cell protein was extracted at the indicated time points (0 to 26 h) after DTB release. The extent of T163 phosphorylation of eIF4A3 was assessed by IPs using anti-FLAG antibody, followed by western blotting with anti-p-eIF4A3 antibody. n = 2.

(B) The mRNA-binding ability of eIF4A3 depending on cell cycle phase; as in (A), except that inducible FLAG-eIF4A3-WT HeLa cells transiently expressing intronless FLuc mRNA and Rβ-8bs-intron reporter mRNA were harvested 0 or 16 h after DTB release. Before cell harvesting, the cells were treated with 150 μM 4SU for 1 h. IPs were performed by means of the anti-FLAG antibody. The levels of coimmunopurified reporter mRNAs were normalized to the level of coimmunopurified FLuc mRNAs. **$p < 0.01$, n = 3.

(C) Interaction between eIF4A3 and CWC22 depending on cell cycle phase; as in (A), except that HeLa cells that stably expressed Dox-inducible FLAG-eIF4A3-WT and transiently expressed MYC-CWC22 were harvested 0 or 16 h after DTB release. n = 2.

(D) Cell cycle profiles analyzed by flow cytometry. HeLa cells that stably expressed Dox-inducible FLAG-eIF4A3-WT, -T163A, or -T163D and were either undepleted or depleted of eIF4A3 were synchronized by single thymidine block (STB). Cell cycle status at the indicated time points was analyzed by FACS. n = 3.

See also Figure S6.

We next repeated the same complementation experiments as performed in Figure 6D and analyzed the levels of endogenous NMD substrates 24 h after cell cycle release (Figure 7C). The levels of endogenous NMD substrates were significantly increased by eIF4A3 downregulation, and this effect was reversed by induction of eIF4A3-WT or -T163A but not eIF4A3-T163D. Therefore, all of these data indicate that maintenance of eIF4A3 phosphorylation causes arrest of the cell cycle at the M-to-G_1 transition and reduces NMD efficiency. Of note, in our GO term enrichment analysis, we identified eight cellular transcripts that are associated with the GO term "regulation of the cell cycle" (Figure S5C). Among them, cyclin-dependent kinase-like 5 (CDKL5) has been reported to function in cell cycle progression after M phase (Barbiero et al., 2017) and to have a single upstream open reading frame in its 5′ UTR: one of NMD-inducing features (Mendell et al., 2004). Indeed, for *CDKL5*, the amount of mRNA relative to its pre-mRNA drastically increased as a result of eIF4A3 phosphorylation in our complementation experiments (Figure 7D). Therefore, these data suggest that *CDKL5* mRNA is one of the endogenous NMD targets, the abundance of which depends on eIF4A3 dephosphorylation for effective M-to-G_1 transition.

DISCUSSION

In this study, we show that eIF4A3 is phosphorylated at T163 by CDK1 and CDK2 in a cell cycle-dependent manner. In addition, we provide molecular evidence that T163 phosphorylation of eIF4A3 contributes to the regulation of EJC assembly and disassembly. Our findings lead us to propose the following model (Figure 7E). In the nucleus, CWC22 preferentially associates with p-eIF4A3, as evidenced by our observations that a greater amount of CWC22 is present in the immunoprecipitate of T163D than in the immunoprecipitate of the T163A or WT version of eIF4A3 (Figures 3 and S3). After delivery of eIF4A3 to the

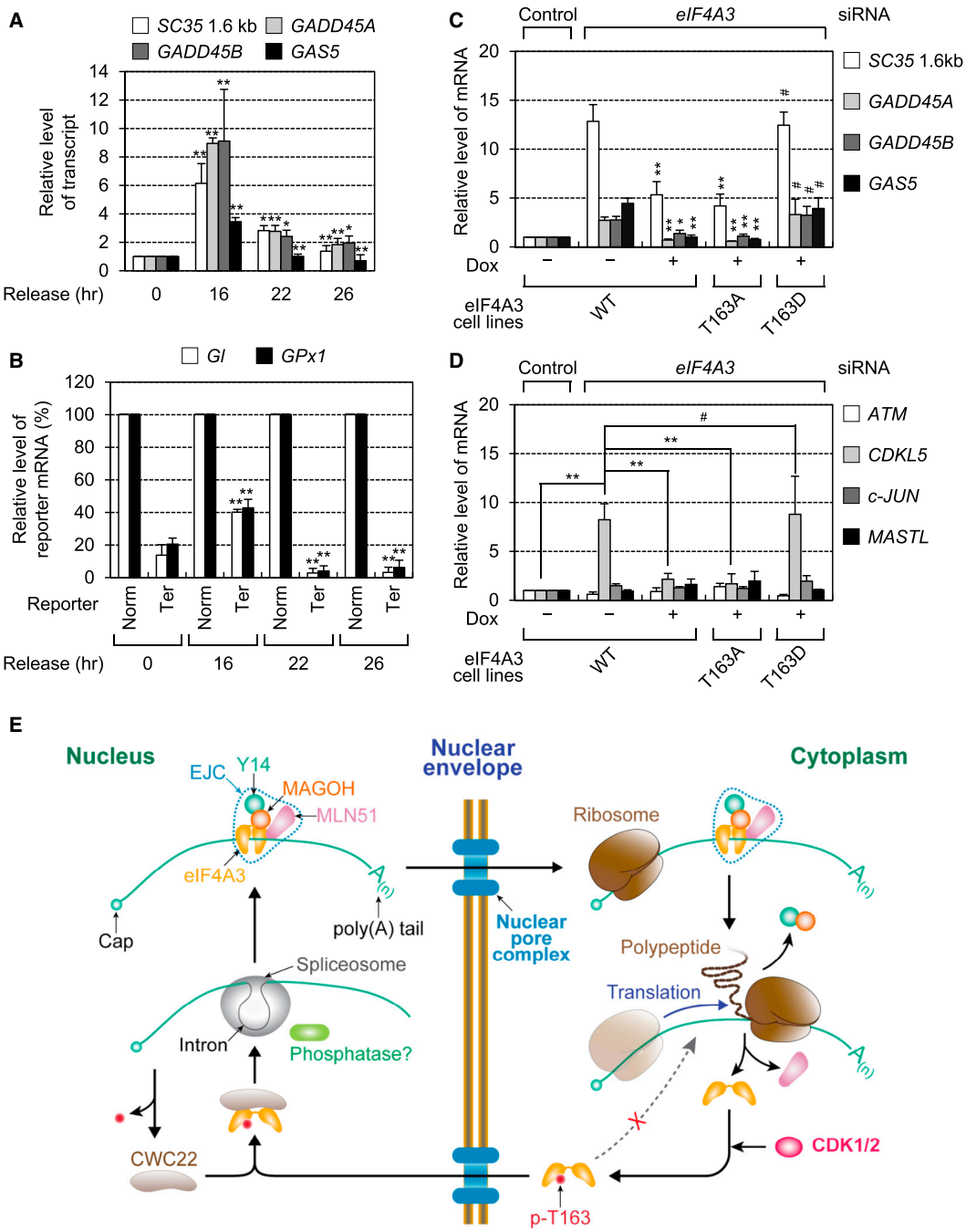

Figure 7. Cell Cycle-Dependent NMD and a Model for EJC Assembly and Disassembly Regulated by T163 Phosphorylation

(A) The levels of newly synthesized endogenous NMD substrates after DTB release. Before harvesting, the cells were treated with 150 μM 4SU for 1 h. The levels of mRNAs were normalized to those of their pre-mRNAs. *$p < 0.05$, **$p < 0.01$, $n = 4$.

(B) NMD of reporter mRNAs (*β-Gl* and *GPx1* mRNAs, either Norm or Ter) after DTB release; as performed in (A), except that exogenously expressed NMD reporter mRNAs were normalized to exogenously expressed *MUP* mRNAs. **$p < 0.01$, $n = 4$.

(C) The effect of eIF4A3 on NMD efficiency depending on cell cycle phase; as in Figure 6D, except that the relative levels of endogenous NMD substrates were analyzed 24 h after an STB release. The levels of mRNAs were normalized to those of their pre-mRNAs. *$p < 0.05$; **$p < 0.01$; #, not significant; $n = 3$.

(D) The effect of eIF4A3 on the levels of transcripts involved in M-to-G_1 transition; as performed in (C), except that, among the eIF4A3-dependent transcripts identified in Figure 5D, previously determined transcripts involved in M-to-G_1 transition were analyzed. The levels of mRNAs were normalized to those of their pre-mRNAs. The level of mRNA of *c-JUN*, one of the intronless mRNAs, was normalized to that of *GAPDH* mRNA. **$p < 0.01$; #, not significant; $n = 3$.

(E) A proposed model for EJC assembly and disassembly regulated by T163 phosphorylation. See Discussion for details.

See also Figure S7.

spliceosome guided by CWC22, eIF4A3 dissociates from CWC22 and associates with mRNA and core components of the EJC (MAGOH, Y14, and MLN51). Because p-eIF4A3 lacks RNA-binding ability (Figures 2 and S2) and fails to form a complex with other core components of the EJC (Figures 3 and S3), efficient EJC formation should be preceded by dephosphorylation of eIF4A3 by an unknown phosphatase.

Disassembly of EJCs occurs during the first (or pioneer) round of translation in the cytoplasm (Maquat et al., 2010; Ryu and Kim, 2017). When a translating ribosome reaches an EJC, ribosome-associated PYM interacts with the Y14-MAGOH complex and destabilizes the interaction between eIF4A3 and Y14-MAGOH (Andersen et al., 2006; Bono et al., 2004, 2006; Gehring et al., 2009). As a consequence, the EJC is displaced from mRNAs and disassembled into two subcomplexes, eIF4A3-MLN51 and Y14-MAGOH, because (1) a significant amount of eIF4A3 is in complex with MLN51 outside of the EJC (Chazal et al., 2013) and (2) Y14 and MAGOH form a stable heterodimer (Fribourg et al., 2003). Because Y14-MAGOH stabilizes the closed conformation of eIF4A3 in the EJC, the eIF4A3 in the eIF4A3-MLN51 subcomplex has an open conformation, which is favorable for CDK1 and CDK2 binding. Considering that (1) the T163D mutant of eIF4A3 fails to associate with all other EJC core components (Figures 3A and S3B) and (2) T163 phosphorylation occurs after EJC disassembly (Figure S3F), it is plausible that CDK1 and CDK2 largely targets eIF4A3 in the eIF4A3-MLN51 subcomplex. When eIF4A3 in the eIF4A3-MLN51 subcomplex is phosphorylated, eIF4A3 eventually dissociates from MLN51 (Figure 3), completing EJC disassembly. This way, T163 phosphorylation of eIF4A3 prevents possible reassembly of an EJC immediately after transient EJC disassembly by a translating ribosome. After complete disassembly of an EJC, all EJC core components are imported into the nucleus for EJC recycling. Of note, T163 phosphorylation does not affect nuclear import of eIF4A3 (Figure S2C).

The continuous cycling of EJC assembly and disassembly mentioned above is likely to be significantly impaired in late M phase. We found that T163 phosphorylation occurs mainly in late M phase (Figures 6A and S6A) and leads to NMD inhibition in this period (Figure 7). We also observed that the T163D mutant of eIF4A3 fails to complement cells depleted of eIF4A3 and causes a delay in M-to-G_1 progression (Figure 6D). Therefore, it is likely that, when the cell is ready to go through M-to-G_1 transition, an unknown phosphatase triggers dephosphorylation of eIF4A3, concomitantly restoring NMD efficiency. Consequently, the cells will pass through M-to-G_1 transition. In this study, we identified *CDKL5* mRNA as one of the plausible NMD substrates, the abundance of which depends on eIF4A3 dephosphorylation for effective M-to-G_1 transition (Figure 7). Presumably, the CDKL5 protein synthesized from the accumulated *CDKL5* mRNA during late M phase may provide a favorable cellular environment for effective M-to-G_1 transition. In addition to NMD, a free EJC component that was detached in late M phase may affect other molecular events, such as alternative splicing or translation mediated by the cap-binding complex, for effective M-to-G_1 transition.

Previous studies and the present one show that (1) a significant amount of p-eIF4A3 remains during interphase (Figures 6A and S6A); (2) the EJC is a multifunctional protein complex that affects splicing, mRNP export, mRNA translation, and mRNA stability (Boehm and Gehring, 2016; Le Hir et al., 2016; Woodward et al., 2017); (3) EJCs are loaded onto other noncanonical regions in addition to the canonical regions ~24 nt upstream of an exon-exon junction (Singh et al., 2012); and (4) free eIF4A3 preferentially promotes translation of mRNAs bound to a nuclear cap-binding complex (Choe et al., 2014; Ryu and Kim, 2017). Therefore, p-eIF4A3 may function in other regulatory pathways during interphase. More complicated than they look, recent data provide growing evidence of noncanonical functions of CDKs in transcription, DNA repair, apoptosis, and cell differentiation (Hydbring et al., 2016). In this regard, future studies should address a variety of biological functions of CDK1 and CDK2-mediated T163 phosphorylation of eIF4A3.

STAR★METHODS

Detailed methods are provided in the online version of this paper and include the following:

- KEY RESOURCES TABLE
- CONTACT FOR REAGENT AND RESOURCE SHARING
- EXPERIMENTAL MODEL AND SUBJECT DETAILS
- METHOD DETAILS
  - Plasmid construction
  - Transfections
  - siRNA sequences
  - Generation of stable cell lines
  - Western blotting
  - IP, RNA-IP, the MBP pull-down assay, and nucleocytoplasmic fractionation
  - Quantitative reverse-transcription PCR analysis
  - Recombinant protein expression and purification
  - *In vitro* kinase assay
  - Liquid chromatography-tandem mass spectrometry (LC-MS/MS)
  - Immunostaining
  - Cell cycle analysis
  - mRNA sequencing
  - CLIP sequencing
  - Processing and mapping of reads
  - Analysis of peak distribution
  - Analysis of eIF4A3-binding sites
  - Consensus motif analysis
  - Analysis of differentially expressed genes (DEGs)
- QUANTIFICATION AND STATISTICAL ANALYSIS
- DATA AND SOFTWARE AVAILABILITY

SUPPLEMENTAL INFORMATION

Supplemental Information includes seven figures and six tables and can be found with this article online at https://doi.org/10.1016/j.celrep.2019.01.101.

ACKNOWLEDGMENTS

We thank Niels Gehring for providing plasmid pCZ-CWC22 and Melisa Moore for pCN-MS2-Y14 and pCN-MS2-MAGOH. This work was supported by a National Research Foundation (NRF) of Korea grant funded by the

Korean government (Ministry of Science, ICT, and Future Planning; NRF-2015R1A3A2033665 and NRF-2018R1A5A1024261), by a Korea University future research grant (K1720051), and by a Korea University grant, South Korea. I.R. and Y.S.W. were supported in part by the NRF funded by the Ministry of Education, Science and Technology, South Korea (NRF-2016R1D1A1B03933894 and NRF-2016R1A6A3A11933515, respectively).

AUTHOR CONTRIBUTIONS

I.R., Y.-S.W., and Y.K.K. designed the experiments, analyzed the data, and wrote the manuscript. I.R. and Y.-S.W. conducted the experiments. H.H. analyzed the NGS data. J.C. acquired and analyzed the mass spectrometry data. M.K.K., D.H.K., and H.K.S. conducted the biochemical experiments. E.K., Y.P., and H.J. conducted the cell biological experiments.

DECLARATION OF INTERESTS

The authors declare no competing interests.

Received: July 23, 2018
Revised: October 16, 2018
Accepted: January 25, 2019
Published: February 19, 2019

REFERENCES

Alexandrov, A., Colognori, D., Shu, M.D., and Steitz, J.A. (2012). Human spliceosomal protein CWC22 plays a role in coupling splicing to exon junction complex deposition and nonsense-mediated decay. Proc. Natl. Acad. Sci. USA *109*, 21313–21318.

Andersen, C.B., Ballut, L., Johansen, J.S., Chamieh, H., Nielsen, K.H., Oliveira, C.L., Pedersen, J.S., Séraphin, B., Le Hir, H., and Andersen, G.R. (2006). Structure of the exon junction core complex with a trapped DEAD-box ATPase bound to RNA. Science *313*, 1968–1972.

Bailey, T.L., Boden, M., Buske, F.A., Frith, M., Grant, C.E., Clementi, L., Ren, J., Li, W.W., and Noble, W.S. (2009). MEME SUITE: tools for motif discovery and searching. Nucleic Acids Res. *37*, W202-8.

Barbiero, I., Valente, D., Chandola, C., Magi, F., Bergo, A., Monteonofrio, L., Tramarin, M., Fazzari, M., Soddu, S., Landsberger, N., et al. (2017). CDKL5 localizes at the centrosome and midbody and is required for faithful cell division. Sci. Rep. *7*, 6228.

Barbosa, I., Haque, N., Fiorini, F., Barrandon, C., Tomasetto, C., Blanchette, M., and Le Hir, H. (2012). Human CWC22 escorts the helicase eIF4AIII to spliceosomes and promotes exon junction complex assembly. Nat. Struct. Mol. Biol. *19*, 983–990.

Bertoli, C., Skotheim, J.M., and de Bruin, R.A. (2013). Control of cell cycle transcription during G1 and S phases. Nat. Rev. Mol. Cell Biol. *14*, 518–528.

Bicknell, A.A., Cenik, C., Chua, H.N., Roth, F.P., and Moore, M.J. (2012). Introns in UTRs: why we should stop ignoring them. BioEssays *34*, 1025–1034.

Boehm, V., and Gehring, N.H. (2016). Exon Junction Complexes: Supervising the Gene Expression Assembly Line. Trends Genet. *32*, 724–735.

Bono, F., Ebert, J., Unterholzner, L., Güttler, T., Izaurralde, E., and Conti, E. (2004). Molecular insights into the interaction of PYM with the Mago-Y14 core of the exon junction complex. EMBO Rep. *5*, 304–310.

Bono, F., Ebert, J., Lorentzen, E., and Conti, E. (2006). The crystal structure of the exon junction complex reveals how it maintains a stable grip on mRNA. Cell *126*, 713–725.

Buchwald, G., Schüssler, S., Basquin, C., Le Hir, H., and Conti, E. (2013). Crystal structure of the human eIF4AIII-CWC22 complex shows how a DEAD-box protein is inhibited by a MIF4G domain. Proc. Natl. Acad. Sci. USA *110*, E4611–E4618.

Chan, W.K., Huang, L., Gudikote, J.P., Chang, Y.F., Imam, J.S., MacLean, J.A., 2nd, and Wilkinson, M.F. (2007). An alternative branch of the nonsense-mediated decay pathway. EMBO J. *26*, 1820–1830.

Chazal, P.E., Daguenet, E., Wendling, C., Ulryck, N., Tomasetto, C., Sargueil, B., and Le Hir, H. (2013). EJC core component MLN51 interacts with eIF3 and activates translation. Proc. Natl. Acad. Sci. USA *110*, 5903–5908.

Chi, Y., Welcker, M., Hizli, A.A., Posakony, J.J., Aebersold, R., and Clurman, B.E. (2008). Identification of CDK2 substrates in human cell lysates. Genome Biol. *9*, R149.

Cho, H., Kim, K.M., Han, S., Choe, J., Park, S.G., Choi, S.S., and Kim, Y.K. (2012). Staufen1-mediated mRNA decay functions in adipogenesis. Mol. Cell *46*, 495–506.

Cho, H., Park, O.H., Park, J., Ryu, I., Kim, J., Ko, J., and Kim, Y.K. (2015). Glucocorticoid receptor interacts with PNRC2 in a ligand-dependent manner to recruit UPF1 for rapid mRNA degradation. Proc. Natl. Acad. Sci. USA *112*, E1540–E1549.

Choe, J., Ryu, I., Park, O.H., Park, J., Cho, H., Yoo, J.S., Chi, S.W., Kim, M.K., Song, H.K., and Kim, Y.K. (2014). eIF4AIII enhances translation of nuclear cap-binding complex-bound mRNAs by promoting disruption of secondary structures in 5'UTR. Proc. Natl. Acad. Sci. USA *111*, E4577–E4586.

Dephoure, N., Zhou, C., Villén, J., Beausoleil, S.A., Bakalarski, C.E., Elledge, S.J., and Gygi, S.P. (2008). A quantitative atlas of mitotic phosphorylation. Proc. Natl. Acad. Sci. USA *105*, 10762–10767.

Dobin, A., Davis, C.A., Schlesinger, F., Drenkow, J., Zaleski, C., Jha, S., Batut, P., Chaisson, M., and Gingeras, T.R. (2013). STAR: ultrafast universal RNA-seq aligner. Bioinformatics *29*, 15–21.

Fribourg, S., Gatfield, D., Izaurralde, E., and Conti, E. (2003). A novel mode of RBD-protein recognition in the Y14-Mago complex. Nat. Struct. Biol. *10*, 433–439.

Gehring, N.H., Lamprinaki, S., Kulozik, A.E., and Hentze, M.W. (2009). Disassembly of exon junction complexes by PYM. Cell *137*, 536–548.

Hachet, O., and Ephrussi, A. (2004). Splicing of oskar RNA in the nucleus is coupled to its cytoplasmic localization. Nature *428*, 959–963.

Hauer, C., Sieber, J., Schwarzl, T., Hollerer, I., Curk, T., Alleaume, A.M., Hentze, M.W., and Kulozik, A.E. (2016). Exon Junction Complexes Show a Distributional Bias toward Alternatively Spliced mRNAs and against mRNAs Coding for Ribosomal Proteins. Cell Rep. *16*, 1588–1603.

Huang, W., Sherman, B.T., and Lempicki, R.A. (2009a). Bioinformatics enrichment tools: paths toward the comprehensive functional analysis of large gene lists. Nucleic Acids Res. *37*, 1–13.

Huang, W., Sherman, B.T., and Lempicki, R.A. (2009b). Systematic and integrative analysis of large gene lists using DAVID bioinformatics resources. Nat. Protoc. *4*, 44–57.

Hug, N., Longman, D., and Cáceres, J.F. (2016). Mechanism and regulation of the nonsense-mediated decay pathway. Nucleic Acids Res. *44*, 1483–1495.

Hydbring, P., Malumbres, M., and Sicinski, P. (2016). Non-canonical functions of cell cycle cyclins and cyclin-dependent kinases. Nat. Rev. Mol. Cell Biol. *17*, 280–292.

Karousis, E.D., Nasif, S., and Mühlemann, O. (2016). Nonsense-mediated mRNA decay: novel mechanistic insights and biological impact. Wiley Interdiscip. Rev. RNA *7*, 661–682.

Kim, Y.K., and Maquat, L.E. (2019). UPFront and center in RNA decay: UPF1 in nonsense-mediated mRNA decay and beyond. RNA, Published online January 17, 2019. https://doi.org/10.1261/rna.070136.118.

Kim, Y.K., Furic, L., Desgroseillers, L., and Maquat, L.E. (2005). Mammalian Staufen1 recruits Upf1 to specific mRNA 3'UTRs so as to elicit mRNA decay. Cell *120*, 195–208.

Kim, K.M., Cho, H., and Kim, Y.K. (2012). The upstream open reading frame of cyclin-dependent kinase inhibitor 1A mRNA negatively regulates translation of the downstream main open reading frame. Biochem. Biophys. Res. Commun. *424*, 469–475.

Le Hir, H., Izaurralde, E., Maquat, L.E., and Moore, M.J. (2000). The spliceosome deposits multiple proteins 20-24 nucleotides upstream of mRNA exon-exon junctions. EMBO J. *19*, 6860–6869.

Le Hir, H., Saulière, J., and Wang, Z. (2016). The exon junction complex as a node of post-transcriptional networks. Nat. Rev. Mol. Cell Biol. *17*, 41–54.

Lejeune, F., Ishigaki, Y., Li, X., and Maquat, L.E. (2002). The exon junction complex is detected on CBP80-bound but not eIF4E-bound mRNA in mammalian cells: dynamics of mRNP remodeling. EMBO J. *21*, 3536–3545.

Li, Q., Imataka, H., Morino, S., Rogers, G.W., Jr., Richter-Cook, N.J., Merrick, W.C., and Sonenberg, N. (1999). Eukaryotic translation initiation factor 4AIII (eIF4AIII) is functionally distinct from eIF4AI and eIF4AII. Mol. Cell. Biol. *19*, 7336–7346.

Maquat, L.E., Tarn, W.Y., and Isken, O. (2010). The pioneer round of translation: features and functions. Cell *142*, 368–374.

Martin, M. (2011). Cutadapt removes adapter sequences from high-throughput sequencing reads. EMBnet J. *17*, 10–12.

Mendell, J.T., Sharifi, N.A., Meyers, J.L., Martinez-Murillo, F., and Dietz, H.C. (2004). Nonsense surveillance regulates expression of diverse classes of mammalian transcripts and mutes genomic noise. Nat. Genet. *36*, 1073–1078.

Nott, A., Le Hir, H., and Moore, M.J. (2004). Splicing enhances translation in mammalian cells: an additional function of the exon junction complex. Genes Dev. *18*, 210–222.

Palacios, I.M., Gatfield, D., St Johnston, D., and Izaurralde, E. (2004). An eIF4AIII-containing complex required for mRNA localization and nonsense-mediated mRNA decay. Nature *427*, 753–757.

Park, O.H., Park, J., Yu, M., An, H.T., Ko, J., and Kim, Y.K. (2016). Identification and molecular characterization of cellular factors required for glucocorticoid receptor-mediated mRNA decay. Genes Dev. *30*, 2093–2105.

Park, J., Park, Y., Ryu, I., Choi, M.H., Lee, H.J., Oh, N., Kim, K., Kim, K.M., Choe, J., Lee, C., et al. (2017). Misfolded polypeptides are selectively recognized and transported toward aggresomes by a CED complex. Nat. Commun. *8*, 15730.

Quinlan, A.R., and Hall, I.M. (2010). BEDTools: a flexible suite of utilities for comparing genomic features. Bioinformatics *26*, 841–842.

Rabani, M., Levin, J.Z., Fan, L., Adiconis, X., Raychowdhury, R., Garber, M., Gnirke, A., Nusbaum, C., Hacohen, N., Friedman, N., et al. (2011). Metabolic labeling of RNA uncovers principles of RNA production and degradation dynamics in mammalian cells. Nat. Biotechnol. *29*, 436–442.

Ryu, I., and Kim, Y.K. (2017). Translation initiation mediated by nuclear cap-binding protein complex. BMB Rep. *50*, 186–193.

Saulière, J., Haque, N., Harms, S., Barbosa, I., Blanchette, M., and Le Hir, H. (2010). The exon junction complex differentially marks spliced junctions. Nat. Struct. Mol. Biol. *17*, 1269–1271.

Saulière, J., Murigneux, V., Wang, Z., Marquenet, E., Barbosa, I., Le Tonquèze, O., Audic, Y., Paillard, L., Roest Crollius, H., and Le Hir, H. (2012). CLIP-seq of eIF4AIII reveals transcriptome-wide mapping of the human exon junction complex. Nat. Struct. Mol. Biol. *19*, 1124–1131.

Schmieder, R., Lim, Y.W., and Edwards, R. (2012). Identification and removal of ribosomal RNA sequences from metatranscriptomes. Bioinformatics *28*, 433–435.

Singh, G., Kucukural, A., Cenik, C., Leszyk, J.D., Shaffer, S.A., Weng, Z., and Moore, M.J. (2012). The cellular EJC interactome reveals higher-order mRNP structure and an EJC-SR protein nexus. Cell *151*, 750–764.

Singh, G., Pratt, G., Yeo, G.W., and Moore, M.J. (2015). The Clothes Make the mRNA: Past and Present Trends in mRNP Fashion. Annu. Rev. Biochem. *84*, 325–354.

Steckelberg, A.L., Boehm, V., Gromadzka, A.M., and Gehring, N.H. (2012). CWC22 connects pre-mRNA splicing and exon junction complex assembly. Cell Rep. *2*, 454–461.

Trapnell, C., Williams, B.A., Pertea, G., Mortazavi, A., Kwan, G., van Baren, M.J., Salzberg, S.L., Wold, B.J., and Pachter, L. (2010). Transcript assembly and quantification by RNA-Seq reveals unannotated transcripts and isoform switching during cell differentiation. Nat. Biotechnol. *28*, 511–515.

Trcek, T., Sato, H., Singer, R.H., and Maquat, L.E. (2013). Temporal and spatial characterization of nonsense-mediated mRNA decay. Genes Dev. *27*, 541–551.

Uren, P.J., Bahrami-Samani, E., Burns, S.C., Qiao, M., Karginov, F.V., Hodges, E., Hannon, G.J., Sanford, J.R., Penalva, L.O., and Smith, A.D. (2012). Site identification in high-throughput RNA-protein interaction data. Bioinformatics *28*, 3013–3020.

van den Heuvel, S., and Harlow, E. (1993). Distinct roles for cyclin-dependent kinases in cell cycle control. Science *262*, 2050–2054.

Woodward, L.A., Mabin, J.W., Gangras, P., and Singh, G. (2017). The exon junction complex: a lifelong guardian of mRNA fate. Wiley Interdiscip. Rev. RNA *8*.

Yepiskoposyan, H., Aeschimann, F., Nilsson, D., Okoniewski, M., and Mühlemann, O. (2011). Autoregulation of the nonsense-mediated mRNA decay pathway in human cells. RNA *17*, 2108–2118.

STAR★METHODS

KEY RESOURCES TABLE

REAGENT or RESOURCE	SOURCE	IDENTIFIER
Antibodies		
Mouse monoclonal anti-eIF4A3	Santa Cruz Biotechnology	Cat#sc-365549; RRID: AB_10847215
Rabbit polyclonal anti-eIF4A3	Cho et al., 2012	N/A
Rabbit polyclonal anti-eIF4A3 (p-T163)	This paper	N/A
Rabbit polyclonal anti-MLN51	Abcam	Cat#ab90651; RRID: AB_2049256
Rabbit polyclonal anti-MAGOH	Abcam	Cat#ab38768; RRID: AB_776156
Mouse monoclonal anti-Y14	Abnova	Cat#MAB2484; RRID: AB_10633684
Rabbit polyclonal anti-PYM	Abcam	Cat#ab108152; RRID: AB_10862121
Mouse polyclonal anti-CWC22	Abnova	Cat#H00057703-B01P; RRID: AB_2087011
Rabbit polyclonal anti-CWC22	Sigma	Cat#SAB1104498
Rabbit polyclonal anti-CBP80	Cho et al., 2012	N/A
Rabbit monoclonal anti-eIF4E	Cell Signaling Technology	Cat#2067; RRID: AB_2097675
Mouse monoclonal anti-FLAG	Sigma	Cat#F3165; RRID: AB_259529
Rat monoclonal anti-HA	Roche	Cat#11867431001; RRID: AB_390919
Mouse monoclonal anti-MYC	Calbiochem	Cat#OP10L; RRID: AB_2266865
Rabbit polyclonal anti-CDK1	Bethyl Laboratories	Cat#A303-663A; RRID: AB_11205291
Rabbit polyclonal anti-CDK2	Bethyl Laboratories	Cat#A301-812A; RRID: AB_1233061
Rabbit polyclonal anti-eIF4A1	Abcam	Cat#ab31217; RRID: AB_732122
Mouse monoclonal anti-β-actin	Sigma	Cat#A5441; RRID: AB_476744
Mouse monoclonal anti-snRNP70	Santa Cruz Biotechnology	Cat#sc-390899
Rabbit polyclonal anti-cyclin B1	Cell Signaling Technology	Cat#4138; RRID: AB_2072132
Rabbit polyclonal anti-cyclin E1	Bethyl Laboratories	Cat#A301-566A; RRID: AB_1039994
Mouse monoclonal anti-cyclin A2	Cell Signaling Technology	Cat#4656; RRID: AB_2071958
Rabbit polyclonal anti-UPF1	Laboratory of Dr. Lynne E. Maquat	N/A
Rabbit polyclonal anti-UPF2	Cho et al., 2012	N/A
Rabbit polyclonal anti-UPF3X	Kim et al., 2012	N/A
Rabbit polyclonal anti-GAPDH	AbFrontier	Cat#LF-PA0018; RRID: AB_1616734
Goat anti-mouse IgG, peroxidase conjugated	Millipore	Cat#AP124P; RRID: AB_90456
Goat anti-rabbit IgG, peroxidase conjugated	Millipore	Cat#AP132P; RRID: AB_90264
Goat anti-rat IgG, peroxidase conjugated	Abcam	Cat#ab6845; RRID: AB_955449
Alexa Fluor® 488-conjugated secondary antibody	Invitrogen	Cat#A-11017; RRID: AB_2534084
Bacterial and Virus Strains		
Escherichia coli Rosetta (DE3) pLysS	Novagen	Cat#70956
Chemicals, Peptides, and Recombinant Proteins		
Plasmocin	Invivogen	Cat#ant-mpt
G418 (Geneticin)	GIBCO	Cat#LS10131027
Puromycin	Sigma	Cat#P8833
Doxycycline	Sigma	Cat#D9891
Thymidine	Sigma	Cat#T9250
4-Thiouridine	Sigma	Cat#T4509
EZ-Link HPDP-Biotin	Thermo Scientific	Cat#21341
4',6-diamidino-2-phenylindole (DAPI)	Biotium	Cat#40011
Bovine serum albumin (BSA)	Bovogen	Cat#BSAS-NZ
3 × FLAG peptides	Sigma	Cat#F4799

(*Continued on next page*)

Continued

REAGENT or RESOURCE	SOURCE	IDENTIFIER
Human His-eIF4A3-WT	Choe et al., 2014	N/A
Human His-eIF4A3-T163A	This paper	N/A
Human CDK1-cyclin B1	Thermo Scientific	Cat#PV3292
Human CDK2-cyclin A2	Thermo Scientific	Cat#PV3267
Human CDK2-cyclin E1	Thermo Scientific	Cat#PV6296
Critical Commercial Assays		
Dynabeads Protein G for Immunoprecipitation	Invitrogen	Cat#10003D
Dynabeads MyOne Streptavidin T1	Invitrogen	Cat#65601
FLAG M2 affinity gel	Sigma	Cat#A2220
rProtein G Agarose 4B	Incospharm	Cat#1105-3
Amylose Resin	NEB	Cat#E8021S
HisTrap HP column	GE Healthcare	Cat#29-0510-21
SMARTer® smRNA-Seq Kit for Illumina®	Clontech	Cat#635031
MycoAlert PLUS Mycoplasma detection kit	Lonza	Cat#LT07-701
Deposited Data		
mRNA-seq and CLIP-seq	This paper	SRP: SRP108397
Mendeley Data dataset	This paper	http://dx.doi.org/10.17632/55t28rfhtc.2
Experimental Models: Cell Lines		
Human: HeLa	ATCC	ATCC number: CCL-2; RRID: CVCL_0030
Human: HEK293T	ATCC	ATCC number: CRL-3216; RRID: CVCL_0063
Oligonucleotides		
siRNA targeting human *CDK1* mRNA: 5′-CAGGU UAUAUCUCAUCUUUGATT-3′	This paper	N/A
siRNA targeting human *CDK2* mRNA: 5′-GGAGC UUGUUAUCGCAAAU-3	This paper	N/A
siRNA targeting human *eIF4A3* mRNA: 5′-CGAGC AAUCAAGCAGAUCA-3	Choe et al., 2014; Palacios et al., 2004	N/A
Nonspecific control siRNA: 5′-ACAAUCCUGAUC AGAAACC-3	Kim et al., 2005	N/A
Oligonucleotides used for plasmid construction	see Table S5	N/A
Oligonucleotides used for qRT-PCRs and semiquantitative RT-PCRs	see Table S6	N/A
Recombinant DNA		
Plasmid: pGL3-Control	Promega	Cat#E1741
Plasmid: p3xFLAG	Sigma	Cat#E7408
Plasmid: pCMV-MYC	Clontech	Cat#635689
Plasmid: pLVX-TRE3G	TaKaRa	Cat#631193
Plasmid: pLVX-TET3G	TaKaRa	Cat#631358
Plasmid: p3xFLAG-eIF4A1	This paper	N/A
Plasmid: p3xFLAG-eIF4A3-WT	Choe et al., 2014	N/A
Plasmid: p3xFLAG-eIF4A3-T163A	This paper	N/A
Plasmid: p3xFLAG-eIF4A3-T163D	This paper	N/A
Plasmid: pcDNA3.1-eIF4A3-WT	This paper	N/A
Plasmid: pcDNA3.1-eIF4A3-T163A	This paper	N/A
Plasmid: pcDNA3.1-eIF4A3-T163D	This paper	N/A
Plasmid: pRSETA-eIF4A3-WT	Choe et al., 2014	N/A
Plasmid: pRSETA-eIF4A3-T163A	This paper	N/A
Plasmid: pRSETA-eIF4A3-T163D	This paper	N/A
Plasmid: FLAG-eIF4A3-WT cell line	This paper	N/A

(*Continued on next page*)

Continued

REAGENT or RESOURCE	SOURCE	IDENTIFIER
Plasmid: FLAG-eIF4A3- T163A cell line	This paper	N/A
Plasmid: FLAG-eIF4A3-T163D cell line	This paper	N/A
Plasmid: Rβ-8bs-intron	Choe et al., 2014	N/A
Plasmid: Rβ-8bs-no intron	Choe et al., 2014	N/A
Plasmid: pMS2-HA-MBP	Choe et al., 2014	N/A
Plasmid: pλN-HA	Cho et al., 2015	N/A
Plasmid: pλN-HA-GFP	Cho et al., 2015	N/A
Plasmid: pMS2-HA	Kim et al., 2005	N/A
Plasmid: pCN-MS2-Y14	Nott et al., 2004	N/A
Plasmid: pλN-HA-Y14	This paper	N/A
Plasmid: pCN-MS2-MAGOH	Nott et al., 2004	N/A
Plasmid: pλN-HA-MAGOH	This paper	N/A
Plasmid: pCMV-CDK1-HA-WT	Addgene	Cat#1888
Plasmid: pCMV-CDK1-HA-DN	Addgene	Cat#1889
Plasmid: pCMV-CDK2-HA-WT	Addgene	Cat#1884
Plasmid: pCMV-CDK2-HA-DN	Addgene	Cat#1885
Plasmid: pOTB7-PYM	Korea Human Gene Bank	Cat#hMU012323
Plasmid: pCMV-MYC-PYM	This paper	N/A
Plasmid: pCZ-CWC22	Steckelberg et al., 2012	N/A
Plasmid: pCMV-MYC-CWC22	This paper	N/A
Plasmid: pmCMV-Gl-Norm	Kim et al., 2005	N/A
Plasmid: pmCMV-Gl-Ter	Kim et al., 2005	N/A
Plasmid: pmCMV-GPx1-Norm	Kim et al., 2005	N/A
Plasmid: pmCMV-GPx1-Ter	Kim et al., 2005	N/A
Plasmid: phCMV-MUP	Kim et al., 2005	N/A
Software and Algorithms		
Cutadapt (v1.12)	Martin, 2011	https://cutadapt.readthedocs.io/en/stable/#
riboPicker (v0.4.3)	Schmieder et al., 2012	http://ribopicker.sourceforge.net/
STAR aligner (v2.5.2b)	Dobin et al., 2013	https://github.com/alexdobin/STAR
Bedtools (v2.25.0)	Quinlan and Hall, 2010	https://bedtools.readthedocs.io/en/stable/#
Cufflinks (v2.2.1)	Trapnell et al., 2010	http://cole-trapnell-lab.github.io/cufflinks/
Piranha (v1.2.1)	Uren et al., 2012	http://smithlabresearch.org/software/piranha/
MEME (v5.0.1)	Bailey et al., 2009	http://meme-suite.org/
Multi Gauge (v3.0)	Fujifilm	N/A
Others		
MaXtract High Density tube	QIAGEN	Cat#12906
RNase-free DNase I	Thermo Scientific	Cat#EN0521
RevertAid Reverse Transcriptase	Thermo Scientific	Cat#EP0441
RiboLock RNase inhibitor	Thermo Scientific	Cat#EO0381
RNase A	Sigma	Cat#R6513
RNase A	Affymetrix	Cat#70194Y
Novex NuPAGE LDS Sample Buffer (4 ×)	Life Technologies	Cat#NP0007
Alkaline phosphatase	Roche	Cat#11800630
T4 PNK	NEB	Cat#M0201L
Proteinase K	Roche	Cat#03115879001
GlycoBlue™	Ambion	Cat#AM9515
Yeast tRNA	Sigma	Cat#R9001

CONTACT FOR REAGENT AND RESOURCE SHARING

Further information and requests for resources and reagents should be directed to and will be fulfilled by the Lead Contact, Yoon Ki Kim (yk-kim@korea.ac.kr).

EXPERIMENTAL MODEL AND SUBJECT DETAILS

The following human cell lines were used in this study: HeLa (sex: female; ATCC) and HEK293T (fetal; ATCC). The cell lines were maintained in Dulbecco's modified Eagle's medium (HyClone) supplemented with 10% (v/v) of fetal bovine serum (HyClone) and 1% (v/v) of a penicillin/streptomycin solution (HyClone) at 37°C and 5% CO_2. To prevent mycoplasma contamination, all cell lines were regularly treated with Plasmocin™ (Invivogen) and tested using the MycoAlert PLUS Mycoplasma detection kit (Lonza) according to manufacturer's instructions.

METHOD DETAILS

Plasmid construction

The following plasmids were previously described or obtained elsewhere: pGL3-Control (Promega); p3xFLAG (Sigma); pCMV-MYC, pLVX-TRE3G, and pLVX-TET3G (Clontech); p3xFLAG-eIF4A3-WT, which expresses human eIF4A3 resistant to *eIF4A3* siRNA, pRSETA-eIF4A3-WT, plasmids Rβ-8bs-intron and Rβ-8bs-no intron, and pMS2-HA-MBP (Choe et al., 2014); pλN-HA and pλN-HA-GFP (Cho et al., 2015); pMS2-HA (Kim et al., 2005); pCN-MS2-Y14 and pCN-MS2-MAGOH (Nott et al., 2004); pCMV-CDK1-HA-WT, pCMV-CDK1-HA-DN, pCMV-CDK2-HA-WT, and pCMV-CDK2-HA-DN [Addgene #1888, #1889, #1884, and #1885, respectively (van den Heuvel and Harlow, 1993)]; pOTB7-PYM (Korea Human Gene Bank; hMU012323); pCZ-CWC22 (Steckelberg et al., 2012); and pmCMV-Gl-Norm and -Ter, pmCMV-GPx1-Norm and -Ter, and phCMV-MUP (Kim et al., 2005).

For the construction of plasmids p3xFLAG-eIF4A3-T163A and -T163D, each fragment containing a mutation was amplified by two-step PCR. First, specific 5′ and 3′ fragments were amplified by PCR using p3xFLAG-eIF4A3-WT as a template and specific oligonucleotides: (i) eIF4A3-F and eIF4A3-T163A-R for the 5′ fragment of T163A, (ii) eIF4A3-T163A-F and eIF4A3-R for the 3′ fragment of T163A, (iii) eIF4A3-F and eIF4A3-T163D-R for the 5′ fragment of T163D, and (iv) eIF4A3-T163D-F and eIF4A3-R for the 3′ fragment of T163D (Table S5). Next, the PCR-amplified fragments corresponding to the 5′ and 3′ fragments were mixed and reamplified by PCR with oligonucleotides for the second PCR: eIF4A3-F and eIF4A3-R (Table S5). The final PCR products digested with BglII and AccI were ligated to linearized p3xFLAG-eIF4A3-WT prepared by digestion with BglII and AccI.

To construct pcDNA3.1-eIF4A3-WT, -T163A, and -T163D, which served as templates for *in vitro* transcription, a fragment of p3xFLAG-eIF4A3-WT, -T163A, or -T163D, which was sequentially treated with NotI, Klenow, and XbaI, was ligated to linearized vector pcDNA3.1-3xFLAG, which was treated sequentially with BamHI, Klenow, and XbaI.

To construct p3xFLAG-eIF4A1, a fragment corresponding to the coding sequence of human eIF4A1 was amplified by PCR using pET28a-eIF4A1 as a template and specific oligonucleotides: eIF4A1-F and eIF4A1-R (Table S5). The PCR-amplified products digested with SalI and BamHI were ligated to linearized plasmid p3xFLAG, which was prepared by digestion with SalI and BamHI.

To construct plasmids pλN-HA-Y14 and pλN-HA-MAGOH, DNA fragments containing the coding sequences of human Y14 and MAGOH were amplified by PCR using pCN-MS2-Y14 and or pCN-MS2-MAGOH, respectively, as a template and specific oligonucleotides: (i) Y14-F and Y14-R for Y14, and (ii) MAGOH-F and MAGOH-R for MAGOH (Table S5). The PCR-amplified fragments digested with EcoRI and XbaI were ligated to linearized vector pλN-HA, which was prepared by digestion with EcoRI and XbaI.

To construct the pCMV-MYC-PYM plasmid, a DNA fragment containing the coding sequence of human PYM was amplified by PCR using plasmid pOTB7-PYM as a template and two specific oligonucleotides: PYM-F and PYM-R (Table S5). The PCR product digested with EcoRI and Acc65I was ligated to linearized plasmid pCMV-MYC, which was prepared by digestion with EcoRI and Acc65I.

For construction of pCMV-MYC-CWC22, a DNA fragment from pCZ-CWC22, which was sequentially treated with XhoI, Klenow, and NotI, was ligated to linearized vector pCMV-MYC, which was sequentially treated with SalI, Klenow, and NotI.

To establish cell lines that stably express inducible FLAG-eIF4A3-WT, -T163A, and -T163D, a DNA fragment containing FLAG-eIF4A3-WT, -T163A, or -T163D was amplified by PCR using p3xFLAG-eIF4A3-WT, -T163A, or -T163D as a template and two specific oligonucleotides: eIF4A3-tet-F and eIF4A3-tet-R (Table S5). The PCR product digested with BamHI and NotI was ligated to pLVX-TRE3G linearized by digestion with BamHI and NotI.

For bacterial expression of recombinant eIF4A3-T163A, pRSETA-eIF4A3-T163A was generated by means of the QuikChange mutagenesis kit (NEB) using pRSETA-eIF4A3-WT as a template with specific oligonucleotides: eIF4A3-T163A-recomb-F and eIF4A3-T163A-recomb-R (Table S5).

Transfections

Cells were transiently transfected with the indicated plasmids or 100 μM *in vitro*-synthesized siRNAs (GenePharma) using Lipofectamine 2000 (Life Technologies; for DNA transfection), Lipofectamine 3000 (Life Technologies; for cell cycle progression after eIF4A3

downregulation), or Oligofectamine (Life Technologies; for siRNA transfection) (Cho et al., 2015; Choe et al., 2014; Park et al., 2016). For DNA transfection into HEK293T cells, the calcium phosphate transfection method was employed.

siRNA sequences

The following siRNA sequences were used for specific downregulation: 5′-r(CAGGUUAUAUCUCAUCUUUGA)d(TT)-3′ (*CDK1* siRNA) and 5′-r(GGAGCUUGUUAUCGCAAAU)d(TT)-3′ (*CDK2* siRNA). The sequences of nonspecific control siRNA (Kim et al., 2005) and *eIF4A3* siRNA (Choe et al., 2014; Palacios et al., 2004) were described previously.

Generation of stable cell lines

To establish Tet-on cell lines, HeLa cells were cotransfected with pLVX-TET3G and pLVX-TRE3G-FLAG-eIF4A3-WT, -T163A, or -T163D. Two days later, the transfected cells were serially diluted and maintained in the normal growth medium containing 600 μg/ml G418 (Geneticin; GIBCO) and 0.2 μg/ml puromycin (Sigma) for 3 weeks. Later, single colonies were isolated and subjected to western blotting for analysis of Dox (Sigma)-dependent expression of the FLAG-eIF4A3 protein. The final cell lines were maintained in the normal growth medium containing 300 μg/ml G418 and 0.1 μg/ml puromycin. For induction of the FLAG-eIF4A3 protein, 50–100 ng/ml Dox was added to the medium.

Western blotting

Primary antibodies against the following proteins served for western blotting or IP: eIF4A3 [Santa Cruz Biotechnology or (Cho et al., 2012)], MLN51 (Abcam), MAGOH (Abcam), Y14 (Abnova), PYM (Abcam), CWC22 (Abnova and Sigma), CBP80 (Cho et al., 2012), eIF4E (Cell Signaling Technology), FLAG (Sigma), HA (Roche), MYC (Calbiochem), CDK1 (Bethyl Laboratories), CDK2 (Bethyl Laboratories), eIF4A1 (Abcam), β-actin (Sigma), snRNP70 (Santa Cruz Biotechnology), cyclin B1 (Cell Signaling Technology), cyclin E1 (Bethyl Laboratories), cyclin A2 (Cell Signaling Technology), UPF1 (a gift from Dr. Lynne E. Maquat), UPF2 (Cho et al., 2012), UPF3X (Kim et al., 2012), and GAPDH (AbFrontier). Secondary antibodies against the primary antibodies were used for western blotting: a peroxidase-conjugated goat anti-mouse IgG antibody and goat anti-rabbit IgG antibody (Millipore) and a peroxidase-conjugated goat anti-rat IgG antibody (Abcam).

A lab-made antibody against phosphorylated T163 of eIF4A3 was raised in rabbits against C-HVVAG(pT)PGRVFDMIR, where pT indicates phospho-threonine. Later, rabbit serum samples were processed by affinity chromatography on immobilized phosphopeptides to purify the antibody.

Signal intensities of bands were quantitated in the Multi Gauge software (version 3.0, Fujifilm).

IP, RNA-IP, the MBP pull-down assay, and nucleocytoplasmic fractionation

IP, RNA-IP, and MBP pull-down assays were performed using HEK293T cells, HeLa cells, or eIF4A3-inducible HeLa Tet-on cell lines. For IP, cells were washed with ice-cold phosphate-buffered saline (PBS) and harvested by centrifugation at 3,000 × *g* for 10 min at 4°C. The pellet was resuspended in 500 μL of NET-2 buffer [50 mM Tris-Cl (pH 7.4), 150 mM NaCl, 1 mM phenylmethylsulfonyl fluoride (Sigma), 2 mM benzamidine hydrochloride (Sigma), 0.05% of NP-40 (IGEPAL® CA-630; Sigma), 10 mM sodium fluoride (Sigma), and 0.25 mM sodium orthovanadate (Sigma)]. The cells in the suspension were ruptured by two rounds of sonication with 30 bursts of 1 s each (output control: 3, duty cycle: 30%; Sonifier 250, Branson), and the lysates were centrifuged at 13,000 × *g* for 10 min at 4°C. The supernatants were precleared with 50 μl of protein G agarose 4B (Incospharm) for 1 h at 4°C. The precleared supernatants were mixed with antibody-conjugated beads or the FLAG M2 affinity gel (Sigma) and incubated for 3 h at 4°C. Later, the beads were washed five times with the NET-2 buffer and resuspended in 100 μl of 2 × sample buffer [10% β-mercaptoethanol, 4% SDS, 100 mM Tris-HCl (pH 6.8), 15% glycerol, and 0.008% bromophenol blue]. Coimmunopurified proteins were analyzed by western blotting.

RNP-IP was performed similarly to IP except (i) the NET-2 buffer was supplemented with 0.2 U/μl RiboLock RNase inhibitor (Thermo Scientific), (ii) the beads were saturated with 10 μg/μl denatured yeast tRNAs (Sigma), (iii) the bound RNAs were extracted using phenol/chloroform/isoamyl alcohol and precipitated with ethanol, and (iv) the resulting RNA samples were analyzed by qRT-PCR.

MBP pull-down assays were conducted by a method similar to RNA-IP except (i) the cells were cross-linked with 0.3% formaldehyde (Sigma) in PBS for 10 min and then quenched with 250 mM glycine (Duchefa) in PBS for 5 min before harvesting and (ii) an amylose resin (NEB) saturated with 10 μg/μl denatured yeast tRNAs was employed instead of the antibody-conjugated resin. Copurified proteins and RNAs were analyzed by western blotting and semiquantitative RT-PCR, respectively.

Nuclear and cytoplasmic fractionation followed by IP or RNA-IP was similar to IP or RNA-IP procedures except (i) the cell pellet was lysed with hypotonic buffer [10 mM Tris-Cl (pH 7.4), 10 mM phenylmethylsulfonyl fluoride, 2 mM benzamidine hydrochloride, 10 mM EDTA, 0.1% Triton X-100 (Sigma), 10 mM sodium fluoride, and 0.25 mM sodium orthovanadate] to obtain the cytoplasmic extracts, (ii) 150 mM NaCl (final concentration) was added to the cytoplasmic extracts before preclearing, and (iii) the beads were washed five times with NET-2 buffer after incubation with the antibody-conjugated resin.

When indicated, the supernatant was treated with 2 μg of RNase A (Sigma) before IP and incubated for 15 min at 37°C.

Quantitative reverse-transcription PCR analysis

Total-cell RNA samples were prepared using the TRIzol Reagent (Life Technologies). Complementary DNAs (cDNAs) were synthesized as described previously (Choe et al., 2014; Park et al., 2017). Briefly, the total-RNA samples were prepared by means of TRIzol (Life Technologies) according to the manufacturer's instructions and digested for 45 min at 37°C with 0.05 U/μl DNase I (Thermo Scientific) supplemented with 0.4 U/μl RNase inhibitor. After purification by means of phenol/chloroform/isoamyl alcohol followed by ethanol precipitation, the RNA samples were denatured by heating at 95°C for 5 min and rapid chilling on ice for 5 min. The denatured RNA samples were subjected to cDNA synthesis for 2 h at 37°C with 6 U/μl RevertAid Reverse Transcriptase (Thermo Scientific) supplemented with 1 U/μl RNase inhibitor according to the manufacturer's instructions. After that, the reverse transcriptase in the reaction was inactivated by heating at 95°C for 5 min. qRT-PCR analysis was performed with gene-specific oligonucleotides (Table S6) and the Light Cycler 480 SYBR Green I Master Mix (Roche) on a Light Cycler 480 II machine (Roche) according to manufacturer's instructions.

To quantify RNAs pulled down by MBP, semiquantitative RT-PCRs were carried out as described elsewhere (Choe et al., 2014). Oligonucleotides for the detection of RLuc mRNA and *GAPDH* mRNA are described in Table S6.

Recombinant protein expression and purification

Purification of recombinant eIF4A3 proteins was described elsewhere (Choe et al., 2014). Briefly, His-eIF4A3-WT or the corresponding T163A mutant was expressed in *Escherichia coli* Rosetta (DE3) pLysS cells by addition of 1 mM isopropyl β-D-1-thiogalactopyranoside (IPTG), when optical density at 600 nm reached 0.5. Next, the cells were incubated for 20 h at 18°C. The cells were then harvested, resuspended in lysis buffer [20 mM 4-(2-hydroxyethyl)-1-piperazineethanesulfonic acid (HEPES)-KOH (pH 7.5), 200 mM KCl, 10% (v/v) glycerol, and 10 mM β-mercaptoethanol], and then sonicated. Total-cell extracts were subjected to affinity purification on a HisTrap HP column (GE Healthcare), and the column was washed with binding buffer [20 mM HEPES-KOH (pH 7.5), 200 mM KCl, 10 mM β-mercaptoethanol, and 10% (v/v) glycerol]. The bound proteins were eluted with 500 mM imidazole dissolved in binding buffer. The purified proteins were dialyzed against a buffer [20 mM HEPES-KOH (pH 7.5), 200 mM KCl, 4 mM DTT, and 10% (v/v) glycerol].

In vitro kinase assay

Recombinant protein complexes CDK1-cyclin B1, CDK2-cyclin A2, and CDK2-cyclin E1 were purchased from Thermo Scientific. The recombinant CDK-cyclin complex (4 nM) or 0.1 μg of bovine serum albumin (BSA; Santa Cruz Biotechnology) was mixed with 0.1 μg of recombinant His-eIF4A3-WT or His-eIF4A3-T163A in the absence or presence of 0.1 mM ATP. After that, the mixtures were incubated for 30 min at 30°C. Then, the samples were analyzed by either western blotting for quantification of the degree of eIF4A3 phosphorylation or silver staining to evaluate the amount of the recombinant proteins.

Liquid chromatography-tandem mass spectrometry (LC-MS/MS)

For proteomic identification of phosphorylated sites in the human eIF4A3 protein, HEK293T cells transiently expressing FLAG-eIF4A3-WT were subjected to IP using an anti-FLAG antibody followed by elution with the 3X FLAG peptide (Sigma) as described elsewhere (Choe et al., 2014). After that, the purified protein was subjected to SDS-PAGE and stained with Coomassie Brilliant Blue. The band containing the FLAG-eIF4A3-WT protein was excised from the gel and isolated for analysis by LC-MS/MS (Diatech).

Immunostaining

Immunostained HeLa cells were examined under an LSM 510 Meta microscope (Carl Zeiss), as described elsewhere (Park et al., 2017). In brief, HeLa cells were transiently transfected with a plasmid expressing FLAG-eIF4A3-WT, -T163A, or -T163D. Two days after transfection, the cells were fixed with 2% paraformaldehyde in PBS and permeabilized with 0.5% Triton X-100 in PBS for 10 min. Distributions of the proteins were visualized with an anti-FLAG primary antibody and an Alexa Fluor® 488-conjugated secondary antibody (Invitrogen). Nuclei were stained with 4′,6-diamidino-2-phenylindole (DAPI; Biotium).

Cell cycle analysis

For synchronization of the cell cycle, cells were first incubated with 2 mM thymidine in the normal growth media for 18 hr. Next, the cells were washed three times with PBS and grown for 8 h in the normal growth medium. Then, the cells were incubated with 2 mM thymidine for 17 hr. After washing with PBS three times and cultivation in the normal growth media, the cells were harvested at various time points (Figures 6A–6C, 7A, and S6A). For cell cycle progression after downregulation of eIF4A3 followed by Dox-mediated induction (Figures 6D and 7B–7D), the stable cell lines were subjected to single thymidine block (STB) by incubation with 2 mM thymidine in the normal growth media for 24 hr. To confirm the status of the cell cycle, small aliquots of the cells were set aside and treated with 0.3 μg/μl RNase A for 30 min at 37°C. Then, the RNase A-treated cells were stained with 50 μg/ml propidium iodide (Sigma) for FACS analysis. FACS was carried out on a BD Accuri™ C6 Plus instrument (BD Biosciences).

To monitor the levels of newly synthesized transcripts, the cells were treated with 150 μM 4-thiouridine (4SU; Sigma) for 1 h before cell harvesting. Purification of 4SU-labeled RNAs was described elsewhere (Rabani et al., 2011). Before purification, EZ-Link Biotin-HPDP (Pierce) had to be dissolved in dimethylformamide (DMF; Sigma) at a concentration of 1 mg/ml. Biotinylation of 4SU-labeled RNAs with 0.2 mg/ml Biotin-HPDP was conducted in biotin-labeling buffer [10 mM Tris-Cl (pH 7.4) and 1 mM EDTA] for 2 h at room temperature. Free Biotin-HPDP was removed by chloroform/isoamyl alcohol (24:1) extraction using a MaXtract High Density tube (QIAGEN), and the biotin-labeled RNA was precipitated with ethanol. The labeled RNA in RNase-free water was incubated with Dynabeads™ MyOne™ Streptavidin T1 beads (Invitrogen) for 15 min at room temperature. After washing, the bound RNA was eluted with 0.1 M dithiothreitol and analyzed by qRT-PCR.

mRNA sequencing

Construction of libraries and sequencing were performed by Macrogen. Total-cell RNAs were obtained from the stable cell lines transfected with either Control siRNA or *eIF4A3* siRNA and either untreated or treated with Dox for 2 days to induce FLAG-eIF4A3-WT or its mutant. The libraries were prepared for 100-bp paired-end sequencing using the TruSeq Stranded mRNA Sample Prep Kit (Illumina). Poly(A)$^+$ RNAs were selectively purified with oligo-d(T)-conjugated magnetic beads. Quality of final cDNA libraries was examined according to the size distribution on an Agilent Bioanalyzer (DNA 1000 kit; Agilent) and by qPCR (Kapa Library Quant Kit; Kapa Biosystems, Wilmington, MA). Sequencing was conducted in paired-end mode (2 × 100 bp) using Illumina HiSeq 2500 (Illumina, CA, USA).

CLIP sequencing

HeLa cells were irradiated with ultraviolet (UV) light (254 nm; 400 mJ/cm^2) by means of a UV cross-linker (UVP) before harvesting. The cross-linked cells were resuspended in 600 μL of lysis buffer [10.8 mM Na_2HPO_4, 3.5 mM KH_2PO_4, 6.8 mM KCl, 342.5 mM NaCl, 0.1% SDS, 0.5% sodium deoxycholate, 0.5% NP-40, 10 mM sodium fluoride, and 0.25 mM sodium orthovanadate, pH 7.2] and incubated for 10 min on ice. RNase-free DNase I (30 U; Thermo Scientific) was added to the cell extracts and incubated at 37°C for 5 min. Then, 0.1 or 5 ng of RNase A (Affymetrix) was added, and the mixture was incubated for additional 10 min at 37°C. After centrifugation at 13,000 × *g* for 20 min at 4°C, the total-cell extracts were subjected to IP using protein G Dynabeads (Invitrogen) conjugated with the anti-FLAG antibody for 2 h at 4°C. The beads were washed three times with lysis buffer and twice with PNK buffer (50 mM Tris-HCl, 10 mM $MgCl_2$, 0.5% NP-40, pH 7.4).

To remove the phosphate groups from the ends of RNAs, the beads were incubated with 0.3 U/μl alkaline phosphatase (Roche) for 10 min at 37°C. After that, the beads were washed twice with PNK+EGTA buffer (50 mM Tris-HCl, 10 mM $MgCl_2$, 0.5% NP-40, 20 mM EGTA, pH 7.4) and twice with PNK buffer. To phosphorylate the 5′ end of RNAs, the beads were incubated with 0.3 U/μl T4 polynucleotide kinase (T4 PNK; NEB) in the presence of 0.1 mM ATP for 10 min at 37°C. Next, the beads were washed three times with PNK+EGTA buffer. Finally, RNAs and proteins bound to the beads were denatured with lithium dodecyl sulfate (LDS) sample buffer (Invitrogen).

To isolate RNA covalently cross-linked to FLAG-eIF4A3 proteins, the samples were subjected to SDS-PAGE in a Novex NuPAGE 10% Bis-Tris gel (Invitrogen), and the separated proteins were transferred to a nitrocellulose membrane. A piece of the membranes corresponding to proteins 40–70 kDa was excised and digested with 4 mg/ml proteinase K (Roche) in PK buffer (100 mM Tris-HCl, 50 mM NaCl, 10 mM EDTA, pH 7.5) for 40 min at 37°C. After that, 7 M urea was added, and the mixture was incubated further for 20 min at 37°C. The soluble fractions were subjected to organic extraction and ethanol precipitation with addition of GlycoBlue™ (Ambion) to precipitate RNA fragments.

Construction of small RNA libraries was carried out using the SMARTer® smRNA-Seq Kit for Illumina® (Clontech). Quality of cDNA libraries was evaluated on an Agilent 2100 BioAnalyzer (Agilent, CA, USA). Sequencing was carried out in paired-end mode (2 × 100 bp) on an Illumina HiSeq 2500 system (Illumina, CA, USA). The sequencing was conducted by Theragene.

Processing and mapping of reads

Throughout this study, only single-end reads corresponding to the sense strand of the input RNA were selected and processed. Before mapping, preprocessing of reads was performed via two steps: trimming of adaptor and poly(A) sequences by means of Cutadapt (Martin, 2011) and removal of ribosomal sequences in the riboPicker software (Schmieder et al., 2012) with a customized rRNA library. During these procedures, the reads with lengths over 15 bp and with Phred quality score over $\geq$ 30 were filtered for further analysis. The processed reads were mapped to the reference human genome (hg19) in the STAR aligner software (Dobin et al., 2013). The reads uniquely mapped to the human genome were selected for subsequent analyses. Pearson's correlation coefficients between two replicates were calculated by means of the NumPy library in Python.

Analysis of peak distribution

To compute the peak distribution across different genomic regions, peak calling was conducted via Piranha (Uren et al., 2012) with settings (-b 20 -a 0.9). Annotation of the exonic regions of mRNAs and ncRNAs was performed in two publicly available databases: RefSeq Genes [hg19; UCSC table browser (http://genome.ucsc.edu/cgi-bin/hgTables)] and GENCODE (Release 19). To obtain the intronic region of those RNAs, the subtractBed module from Bedtools v.2.25.0 was used (Quinlan and Hall, 2010). The mapped reads were assigned to each genomic region category using the intersectBed function from Bedtools. Seven hierarchical categories were

set up according to the following annotation: CDSs > 5′UTRs > 3′UTRs > lncRNAs > introns of mRNAs > intron of lncRNAs > No annotation. These categories are a modification of a method described previously (Saulière et al., 2010). To calculate peak enrichment in each category, the number of peaks was divided by the size of the corresponding region.

Analysis of eIF4A3-binding sites

To explore eIF4A3-binding sites located in the exons of CDSs, multiexon mRNAs (the number of exons > 3) from RefSeq were employed. Among alternative forms of the same gene, the longest one was selected as a representative with more than 1 FPKM (fragments per kilobase of transcript per million mapped reads) from our mRNA sequencing data. The normalized expression values were calculated by means of the Cufflinks pipeline (Trapnell et al., 2010). The center of uniquely mapped reads upstream of exon-exon junctions was analyzed in different exons of the coding regions. The results were visualized using Kernel Density Estimation. To ascertain the distributional differences among eIF4A3-WT, T163A, and T163D, the Kolmogorov-Smirnov test implemented in the scipy.stats.ks_2samp module of the SciPy Python library was applied to statistical analysis.

For the analysis of eIF4A3-binding sites located in the introns, the centers of the overlapping peaks mapped to introns were determined using the data from the CLIPs of eIF4A3-WT, -T163A, and -T163D. The intersectBed option of Bedtools was applied to mask the peaks mapped to alternative exons within intronic regions. For comparison, the 2,000 positions located in intronic regions were randomly selected using random.permutation and random.choice modules of the Python NumPy library.

To determine whether T163 phosphorylation of eIF4A3 affects its binding to exons of protein-coding genes at the transcriptome level, the peaks or reads mapped to exons of protein-coding genes were classified into two categories: (i) canonical peaks or reads, the centers of which were located between 40 and 10 nucleotides upstream of the exon-exon junctions, and (ii) noncanonical peaks or reads with their centers outside the canonical regions of exons. To determine the percentages of canonical and noncanonical peaks according to different thresholds, canonical or noncanonical overlapping peaks were obtained from CLIP1 and CLIP2 data by means of Piranha (-b 20 -a 0.85).

To explore changes in the abundance of the reads mapped to an individual canonical or noncanonical exonic region upon T163 phosphorylation at the genome-wide level, the reads (RPMs $\geq$ 1.0) mapped to canonical or noncanonical exonic regions were first selected from the data of eIF4A3-WT CLIPs. Then, the mean values of RPMs obtained from the CLIPs of eIF4A3-T163A or -T163D were normalized to those of the WT and presented on the $\log_{10}$ scale. To avoid division by zero, an arbitrary pseudo-count (0.001) was added before normalization.

Consensus motif analysis

To discover potential consensus motifs, the MEME (v.5.0.1) algorithm was executed using the top 1,000 canonical and noncanonical overlapping peaks from the CLIPs of eIF4A3-WT and -T163A, respectively (Bailey et al., 2009). The motif length was restricted to 6–8 nucleotides. Finally, the consensus motif with the lowest *E* value was selected as the representative. In T163D CLIP, we obtained only 47 canonical and 440 noncanonical peaks. Because of the insufficient number of the peaks, we could not discover a significant consensus motif by means of T163D CLIP data.

Analysis of differentially expressed genes (DEGs)

Gene expression was quantified in FPKM by means of mRNA sequencing data in Cufflinks version 2.2.1 (Trapnell et al., 2010). DEGs (either upregulated or downregulated at least 1.5-fold after eIF4A3 downregulation; $p < 0.05$) were detected by the Cuffdiff program, a part of the Cufflinks software package (Table S2). Among those DEGs, we assessed only a DEG group including the genes whose expression change was reversed by Dox-mediated induction of FLAG-eIF4A3-WT (at least 1.5-fold; $p < 0.05$; Table S3).

For GO evaluation, the DEG group was uploaded to DAVID (Huang et al., 2009a, 2009b) and then analyzed with the functional annotation tool. The output file was downloaded, and then GO terms and their corresponding *P* values were acquired.

To evaluate the expression of NMD substrates in the DEG group, we used the list of endogenous NMD substrates evaluated experimentally in another report (Yepiskoposyan et al., 2011). The list of NMD substrates consisted of 157 genes (judging by gene symbols) that were significantly upregulated in both UPF1- and SMG6-depleted HeLa cells. Of these, 123 genes with a nonzero FPKM value were matched with the genes in our dataset, among which 40 genes were found to be upregulated by the eIF4A3 downregulation and to undergo reversal of expression under the influence of Dox-mediated induction of FLAG-eIF4A3-WT in our DEG group. The two-sided t test implemented in the scipy.stats.ttest in a module of the SciPy Python library was applied to statistical analysis.

QUANTIFICATION AND STATISTICAL ANALYSIS

In most cases, data obtained from three or four biological replicates were analyzed, unless indicated otherwise in the Figure legends. Statistical significance defined as a *P* value < 0.05 or < 0.01 was determined by two-tailed and equal-variance Student's t test. Data are presented as the mean ± standard deviation. In case of cumulative distribution function analysis, statistical significance was determined by the two-tailed Mann-Whitney *U* test. For the analysis of correlation between mRNA sequencing data of two biological replicates, Pearson's correlation coefficients (*r*) were calculated. To assess the distribution of the centers of uniquely mapped reads

with reference to the 3′ ends of the exons of CDSs, *P* values were calculated by the two-sided Kolmogorov-Smirnov test. To assess the relative number of RPMs of reads mapped to an individual canonical and noncanonical region, *P* values were calculated by the one-tailed Mann-Whitney *U* test.

DATA AND SOFTWARE AVAILABILITY

The accession number for poly(A)+ RNA-seq and CLIP-seq in this paper is SRP: SRP108397. Raw data images can be found at http://dx.doi.org/10.17632/55t28rfhtc.2.